

Taylor & Francis
Taylor & Francis Group

Combustion Science and Technology

ISSN: 0010-2202 (Print) 1563-521X (Online) Journal homepage: www.tandfonline.com/journals/gcst20

Experimental Demonstration of Detonation Initiation in a Rotating Detonation Engine by Laser Ignition

Tomoyuki Sato , Michael Börner , Wolfgang Armbruster , Alexander Bee , Maria Giulia Monti & Justin Hardi

To cite this article: Tomoyuki Sato , Michael Börner , Wolfgang Armbruster , Alexander Bee , Maria Giulia Monti & Justin Hardi (07 Oct 2026): Experimental Demonstration of Detonation Initiation in a Rotating Detonation Engine by Laser Ignition, Combustion Science and Technology, DOI: 10.1080/00102202.2026.2741666

To link to this article: https://doi.org/10.1080/00102202.2026.2741666

© 2026 The Author(s). Published with license by Taylor & Francis Group, LLC.

Published online: 07 Oct 2026.

Submit your article to this journal

View related articles

View Crossmark data

Full Terms & Conditions of access and use can be found at
https://www.tandfonline.com/action/journalInformation?journalCode=gcst20

COMBUSTION SCIENCE AND TECHNOLOGY
https://doi.org/10.1080/00102202.2026.2741666

Taylor & Francis
by informa

OPEN ACCESS Check for updates

Experimental Demonstration of Detonation Initiation in a Rotating Detonation Engine by Laser Ignition

Tomoyuki Sato, Michael Börner, Wolfgang Armbruster, Alexander Bee, Maria Giulia Monti, and Justin Hardi

Institute of Space Propulsion, German Aerospace Center (DLR), Hardthausen am Kocher, Germany

ABSTRACT

Rotating detonation engines (RDEs) are considered promising next-generation propulsion systems, and several ignition methods have been employed to start them. Although laser ignition has attracted considerable attention and has been applied in various aerospace applications, its application to RDEs remains largely unexplored. Therefore, this study aims to demonstrate the feasibility of laser ignition for RDEs. A series of experiments was conducted using laser ablation ignition (LAI) and laser-induced spark ignition (LSI) with gaseous hydrogen and oxygen over total mass flow rates of 17.1–61.5 g/s and equivalence ratios of 0.74–1.89. Ignition success was achieved in all 29 test cases without significant structural degradation of the ignition system or combustion chamber. Detonation initiation success was evaluated using two criteria: a non-dimensional propagation velocity of the rotating chemiluminescence pattern greater than 0.6 and a non-dimensional maximum fill height of the unburned gas greater than 3. In the LAI configuration, both criteria were satisfied at four operating conditions corresponding to total mass flow rates of 32.1–45.0 g/s and equivalence ratios of 0.85–0.98 and 1.32. In the LSI configuration, the non-dimensional velocities were comparable to those in the LAI cases over the tested range of total mass flow rates, and both criteria were satisfied at a total mass flow rate of 35.6 g/s and an equivalence ratio of 0.97. Therefore, successful operation of the laser-ignited RDE was demonstrated for both LAI and LSI under the respective operating conditions.

ARTICLE HISTORY
Received 21 April 2026
Revised 4 September 2026
Accepted 26 September 2026

KEYWORDS
Rotating detonation engine; laser ablation ignition; laser-induced spark ignition; detonation initiation; flame kernel development

Introduction

Detonation is a self-sustaining supersonic combustion wave (Wolański 2013). In a detonation wave, leading shock waves compress the unburned gas adiabatically, thereby increasing its temperature and pressure to initiate chemical reactions (Döring 1943). Rotating detonation engine (RDE) is one of the major applications of the detonation phenomenon (Nicholls et al. 1966). In conventional RDEs, single or multiple detonation waves propagate in an annular, cylindrical, or plane-radial channel at frequencies of 1–50 kHz to generate continuous thrust (Voitsekhovskii 1960). Owing not only to their high-speed propagation but also to their lower entropy generation compared with the conventional combustion mode, namely deflagration, RDEs are considered a promising propulsion

CONTACT Tomoyuki Sato tomoyuki.sato@dlr.de Institute of Space Propulsion, German Aerospace Center (DLR), Im Langen Grund, Hardthausen am Kocher 74239, Germany

© 2026 The Author(s). Published with license by Taylor & Francis Group, LLC.
This is an Open Access article distributed under the terms of the Creative Commons Attribution License (http://creativecommons.org/licenses/by/4.0/), which permits unrestricted use, distribution, and reproduction in any medium, provided the original work is properly cited. The terms on which this article has been published allow the posting of the Accepted Manuscript in a repository by the author(s) or with their consent.

concept because they can provide compact and simple-structured combustors with high theoretical thermal efficiency (Kailasanath 2000).

Generally, RDEs are started using pre-detonators (Armbruster et al. 2025). In addition, various other methods have been investigated, including spark plugs (Kindracki et al. 2011), high-voltage discharges (Yang et al. 2016), glow plugs (Michalski et al. 2024), torch igniter or thermal jets (Stevens et al. 2021; Bai et al. 2023), hypergolic propellants (Anderson et al. 2020), gunpowder (Goto et al. 2023), and exploding wires (Bykovskii et al. 1994). Nevertheless, each method has its own limitations, restricting the practical application of RDEs in aerospace systems. For example, gunpowder and exploding wires are one-time ignition methods, preventing repeated engine restarts. Although other methods provide restart capability, additional feed lines and combustion chambers are required for pre-detonators, torch igniters, and hypergolic propellants, resulting in increased system weight for aerospace vehicles. Spark plugs and glow plugs can avoid these system-level challenges; however, they face other challenges. For example, because their energy deposition lasts on the order of 0.1–1 ms, the initial flame kernel can experience noticeable deformation or displacement (Endo et al. 2018). Moreover, because the flame kernel is formed in the vicinity of electrodes, heat losses to the electrodes and surrounding flow can impede flame development or even cause quenching (Pretto et al. 2024).

As a potential ignition technology for RDEs, this study focuses on laser ignition, especially laser ablation ignition (LAI) and laser-induced spark ignition (LSI). In LAI, a laser beam is focused onto the surface of a target, generating an ablation plasma composed of vaporized target material and surrounding gas, which serves as the ignition source (Takahashi and Kato 2021). In LSI, on the other hand, the beam is focused into a highly localized focal region in the combustible mixture. The laser power density reaches 10^{10}–10^{11} W/cm^2, generating a breakdown plasma that initiates chemical reactions (Morgan 1975). LAI is more advantageous in terms of energy requirement because the minimum ignition energy for GH_2/GOx mixture in LAI is approximately 10% of that in LSI (Mori et al. 2003), whereas LSI provides greater flexibility in selecting the ignition location. Additionally, in both LAI and LSI, energy deposition is completed on the order of nano-seconds, and the initial flame kernel is generated on the order of 10–100 μs (Ronney 1994). Therefore, even in turbulent flows, deformation and displacement of the initial flame kernel can be mitigated, preventing flame quenching or misfire. Owing to these features, especially in aerospace applications where accurate and active ignition timing control is required, laser ignition has been implemented in rocket motors (Morishita et al. 2022), liquid rocket engines (Liou 1984; Börner et al. 2017), and scramjet engine models (Brieschenk et al. 2013; Li et al. 2017). Nonetheless, to the best of the authors' knowledge, no previous study has investigated laser ignition as a starting method for RDEs, and thus the viability of laser ignition for RDE applications remains unclear.

Since this is a demonstrative study, the main objective of this paper is to demonstrate the successful operation of a laser-ignited RDE, and particular emphasis has been placed on assessing whether rotating detonation waves were established. Although benchmarking against conventional ignition methods is important for evaluating the advantages of laser ignition, the objective of the present study is limited to demonstrating the feasibility of laser ignition. Other related aspects, e.g. systematic comparisons with conventional ignition methods under identical operating conditions and transient detonation initiation and propagation characteristics, are beyond the scope of the present study and will be addressed

in future work. In this study, a series of experiments was performed using LAI and LSI with gaseous hydrogen and oxygen at different total mass flow rates and equivalence ratios. To characterize detonation propagation, pressure and light intensity fluctuations inside the combustion chamber were measured in addition to high-speed chemiluminescence visualization. In the analysis, because the minimum operating conditions required to sustain rotating detonation waves have not yet been fully established, detonation propagation under stable operating conditions was assessed using two indicators: the non-dimensional propagation velocity of the rotating chemiluminescence pattern and non-dimensional maximum fill height of unburned gas. The results of this assessment were then used to evaluate the detonation initiation success and thereby demonstrate the successful operation of the laser-ignited RDE.

Methodology

Experimental apparatus

The cross-sectional schematic of the RDE used in the experimental campaign is shown in Figure 1 together with a cylindrical coordinate system. The longitudinal axis, z, was defined such that $z = 0$ mm was located at the injector plate surface, with the positive direction toward the chamber exit, and the radial axis, r, was defined from the inner body toward the

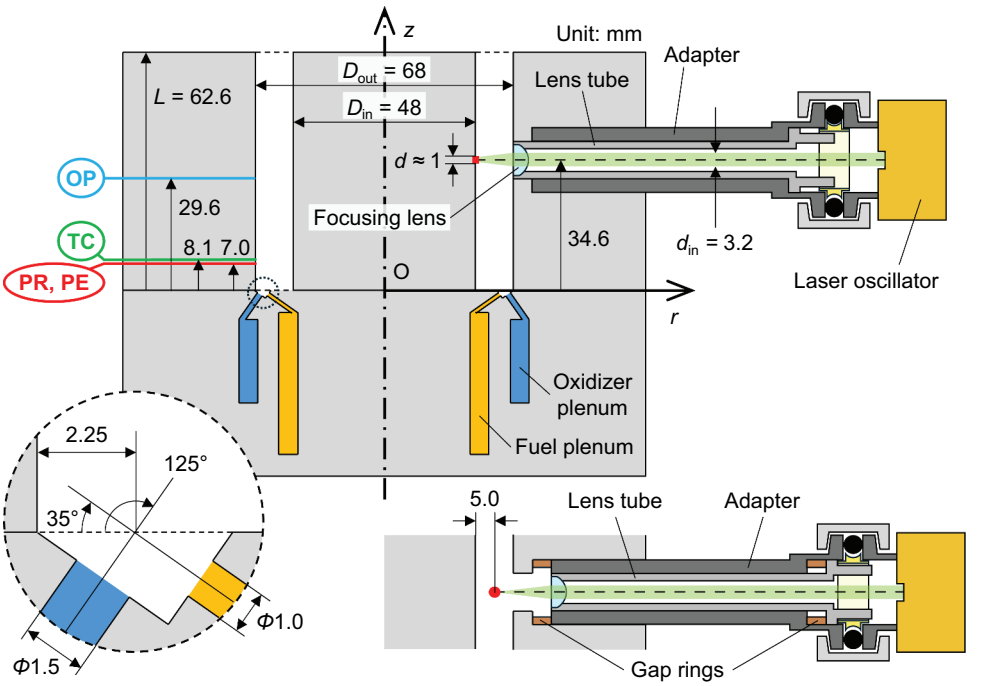


Figure 1. Overview of the experimental configurations: cross-sectional views of the RDE in the LAI setup (top) and LSI setup (bottom right), and an enlarged view of a pair of injection holes (bottom left). Sensors are abbreviated as follows: OP = optical probe; TC = thermocouple; PR = piezo-resistive pressure sensor; PE = piezo-electric pressure sensor. Note that the laser beam is illustrated in green for visibility, although its actual wavelength was 1064 nm.

outer wall. The annular channel had an outer diameter of $D_{out} = 68$ mm, an inner diameter of $D_{in} = 48$ mm, and a length of $L = 62.6$ mm. The chamber bottom contained 72 pairs of injection holes designed for 90-degree impingement: the inner holes have a diameter of 1.0 mm and an inclination angle of 35 degrees relative to the r-axis, whereas the outer holes have a diameter of 1.5 mm and an inclination angle of 125 degrees, as shown in Figure 1 (bottom left). The inner holes supplied the fuel, and the outer holes supplied the oxidizer, such that the jet centerlines were intended to interact at $z = 0$ mm.

The laser configurations for LAI and LSI are shown in the top and bottom-right panels of Figure 1, respectively. A laser oscillator (HiPoLas Gen-V Laser Ignition System, SAL) (Kroupa and Börner 2019; Kroupa et al. 2024) was mounted on an adapter attached to the outer body of the RDE at $z = 34.6$ mm. This axial position was selected based on the expected axial extent of the rotating detonation wave to mitigate the thermal load on the focusing lens located at the tip of the lens tube. In a previous test campaign (Armbruster et al. 2026) using the same RDE equipped with an optically accessible quartz window, the axial extent of the detonation wave was found to be approximately 10 mm at total mass flow rates of 48.5 and 50 g/s and equivalence ratios of 0.84 and 0.76. Based on these observations and manufacturing constraints, the mounting position of laser igniter was determined.

The laser beam configuration was characterized by the following parameters: wavelength $\Lambda = 1064$ nm, input beam diameter $d_{in} = 3.2$ mm, pulse energy $E_{in} = 33.7 \pm 0.8$ mJ, pulse width (FWHM) $\Delta t_{FWHM} = 2.5$ ns, and beam quality factor $M^2 = 3$. The corresponding laser peak power was 1.3×10^7 W, and the incident power density was 1.7×10^8 W/cm^2. The beam was focused by a lens with a focal length of $l_F = 15$ mm mounted at the tip of the lens tube. The focal position in the radial direction was adjusted using gap rings placed between the outer body, the adapter, and the lens tube. In LAI, as shown in Figure 1 (top), the focusing lens was flush-mounted with the outer channel wall so that the beam was focused to a spot approximately 1 mm in diameter on the inner body surface. In contrast, in LSI, as shown in Figure 1 (bottom right), the focusing lens was recessed using gap rings, and the beam was focused at a point located 5 mm from the inner body surface. Assuming a Gaussian beam with the aforementioned laser parameters, the beam waist diameter, d_0, can be estimated using the following equation (Saleh and Teich 2019):

$$d_0 = \frac{4M^2 \Lambda l_F}{\pi d_{in}} \tag{1}$$

The focused beam diameter, d, is given as a function of the distance from the beam waist, l, as follows:

$$d(l) = d_0 \sqrt{1 + \left(\frac{l}{l_R}\right)^2} \tag{2}$$

where, l_R is the Rayleigh length, given by:

$$l_R = \frac{\pi d_0^2}{4M^2 \Lambda} \tag{3}$$

Using Eqs. (1)–(3), the theoretical beam diameter at the ignition point was estimated to be $d = 1.1$ mm for LAI and 19.1 µm for LSI, corresponding to the beam waist diameter ($d = d_0$). Because the actual beam diameter was not measured, these values should be regarded as theoretical estimates based on the Gaussian beam model.

The time-averaged temperature and pressure within the combustion chamber were measured using a type-K thermocouple (Electronic Sensor) at $z = 8.1$ mm and a piezo-resistive pressure sensor (4043A, Kistler) at $z = 7.0$ mm. Both measurements were acquired at a sampling rate of 1 kHz. To characterize detonation propagation, three additional measurements were conducted. First, a piezo-electric pressure sensor (603CAA, Kistler) was installed at $z = 7.0$ mm to measure the pressure fluctuations associated with detonation propagation at a sampling rate of 4 MHz. Second, an optical probe was installed at $z = 29.6$ mm to measure the chemiluminescence intensity fluctuations. The probe consists of a hollow cylinder connected to an optical fiber that transmitted the light emitted by deflagration or detonation. The light was converted into an electric signal by a photomultiplier at 4 MHz. Third, to determine the number and propagation direction of the rotating detonation waves, the chemiluminescence emitted within the channel was visualized using a high-speed camera (SA-Z type 2100K, Photron) from the combustor exit. The spatial resolution was set to 256×256 pixels, and images were recorded at a frame rate of 180 kHz with an exposure time of 3.75 μs.

The mass flow rates of the fuel and oxidizer were measured using Coriolis mass flowmeters (CMF025M, Micro Motion) at a sampling rate of 11.4 Hz. Because this sampling rate was lower than those of the other measurements and insufficient to resolve the instantaneous mass flow rates immediately before ignition, the measured mass flow rates, $\dot{m}$, were compensated using the isentropic flow equation with a discharge coefficient determined from the measured mass flow rates, as follows:

$$\dot{m}_c = C_d(\dot{m}) \cdot \frac{p_0 A}{\sqrt{RT_0}} \sqrt{\gamma \left(\frac{2}{\gamma+1}\right)^{\frac{\gamma+1}{\gamma-1}}} \tag{4}$$

$$\dot{m}_c = C_d(\dot{m}) \cdot \frac{p_0 A}{\sqrt{RT_0}} \sqrt{\frac{2\gamma}{\gamma-1}\left\{\left(\frac{p_{cc}}{p_0}\right)^{\frac{2}{\gamma}} - \left(\frac{p_{cc}}{p_0}\right)^{\frac{\gamma+1}{\gamma}}\right\}} \tag{5}$$

where $\dot{m}_c$ is the compensated mass flow rate, C_d is the discharge coefficient determined from the measured mass flow rate, A is the total injection area, R and γ are the gas constant and specific heat ratio of the propellant, p_0 and T_0 are the plenum pressure and temperature, and p_{cc} is the combustion chamber pressure. Equation (4) was applied under choked-flow conditions when the pressure ratio between the combustion chamber and the plenum was below the following critical value, Π:

$$\Pi \equiv \frac{p_{cc}}{p_0} = \left(\frac{2}{\gamma+1}\right)^{\frac{\gamma}{\gamma-1}} \tag{6}$$

Experimental conditions

Gaseous hydrogen and oxygen were used as the fuel and oxidizer, respectively. The ignition method, number of repetitions, total mass flow rate, $\dot{m}_{total}$, and equivalence ratio, ER, were varied as summarized in Table 1. Here, the non-dimensional parameter ROF denotes the mass-based oxidizer-to-fuel ratio, $ROF = \dot{m}_{ox}/\dot{m}_{fu}$. The symbols (B) and (S) denote 50 Hz burst laser emission and single-pulse emission, respectively. The burst mode was mainly used during the initial trials to avoid misfire. The elapsed time from run-valve opening to laser triggering, Δt_{trg}, was also adjusted to minimize the amount of propellant released into the test facility while ensuring that ignition occurred under stable operating conditions.

Table 1. Summary of the operating conditions.

Method × Repetition	$\dot{m}_{total}$ [g/s]	*ER* [-]	*ROF* [-]	Δt_{trg} [ms]
LAI (B) × 3	36.0 ± 1.0	0.98 ± 0.16	8.1 ± 1.6	144
LAI (S) × 3	26.8 ± 0.6	0.96 ± 0.13	8.3 ± 1.3	300
LAI (S) × 3	17.7 ± 0.6	0.96 ± 0.25	8.3 ± 2.8	300
LSI (B) × 3	35.6 ± 1.0	0.97 ± 0.13	8.2 ± 1.2	144
LSI (S) × 3	26.4 ± 0.5	0.95 ± 0.12	8.4 ± 1.2	300
LSI (S) × 3	17.1 ± 0.6	0.86 ± 0.22	9.2 ± 3.1	300
LAI (S) × 1	32.1 ± 0.7	0.92 ± 0.12	8.6 ± 1.2	300
LAI (S) × 1	44.8 ± 1.1	0.93 ± 0.13	8.5 ± 1.3	144
LAI (S) × 1	55.6 ± 0.9	0.91 ± 0.10	8.8 ± 1.0	144
LAI (S) × 1	61.5 ± 0.6	0.99 ± 0.06	8.0 ± 0.5	144
LAI (S) × 1	46.3 ± 0.9	0.74 ± 0.08	10.7 ± 1.2	144
LAI (S) × 1	45.0 ± 1.2	0.85 ± 0.13	9.4 ± 1.6	144
LAI (S) × 1	44.7 ± 0.9	1.12 ± 0.11	7.1 ± 0.8	144
LAI (S) × 1	44.4 ± 0.9	1.25 ± 0.14	6.3 ± 0.8	144
LAI (S) × 1	44.9 ± 0.9	1.32 ± 0.12	6.0 ± 0.6	144
LAI (S) × 1	44.1 ± 0.9	1.59 ± 0.10	5.0 ± 0.3	144
LAI (S) × 1	44.5 ± 0.8	1.89 ± 0.08	4.2 ± 0.2	144

The experimental campaign began with the LAI configuration. The target total mass flow rates were $\dot{m}_{total}$ = 18, 27, and 36 g/s, while the target equivalence ratio was fixed at *ER* = 1.0. These operating conditions were expected to lie near the boundary between the deflagrative and detonative operating modes of the present RDEs (Yang et al. 2016). Three trials were conducted at each mass flow rate to evaluate the repeatability of the experiments. Next, the LSI configuration was tested under the same target operating conditions to investigate the differences from LAI during the initial phase and steady state operation. Similar to the LAI tests, three trials were conducted with LSI configuration at each mass flow rate. Finally, using the LAI configuration, the total mass flow rate and equivalence ratio were varied over the ranges of $\dot{m}_{total}$ = 32.1 – 61.5 g/s and *ER* = 0.74 – 1.89. Each operating condition was tested once, resulting in a total of 29 test cases. All tests were conducted at an ambient temperature of 283 ± 2 K and an ambient pressure of 95.9 ± 0.6 kPa.

Results and discussion

Ignition success was achieved in all 29 test cases; no misfire or flame quenching occurred, and the propellants were reliably lit, resulting in sustained combustion. In particular, in the burst-mode tests, ignition was successfully achieved following the first laser pulse. The piezo-electric pressure sensor failed during the tests at $\dot{m}_{total}$ = 46.3 and 45.0 g/s (*ER* = 0.74 and 0.85); therefore, the pressure data from these cases were excluded from the analysis. To demonstrate the successful operation of the laser-ignited RDE, the following analyses were performed. First, the integrity of the laser ignition system was investigated. Second, the overall flowfield evolution and the immediate post-ignition flowfield evolution were characterized. Third, and most importantly, detonation propagation under stable operating conditions was assessed, and the detonation initiation success was subsequently evaluated using the assessment results. Finally, a simplified model was developed to explain the ignition success. For clarity, throughout this paper, ignition success refers to the successful establishment of combustion by laser ignition, whereas detonation initiation success refers specifically to the establishment of a rotating detonation wave.

Integrity of the laser ignition system

No failure of the optical system was observed throughout the test campaign, and the focusing lens remained free of cracks or other visible damage. On the other hand, a laser-ablation mark was observed on the inner-body surface at the axial position corresponding to the laser igniter, as shown in Figure 2. The diameter of the ablation mark was $d = 1.5 \pm 0.1$ mm, which was consistent with the previously estimated value based on the Gaussian beam model, whereas the crater depth was too shallow to measure. Instead, the following three characteristic depths were estimated: the skin depth, the theoretical melt depth, and the thermal diffusion length.

First, the optical skin depth, δ_{opt}, which corresponds to the optical penetration depth, can be estimated by the following equation:

$$\delta_{\mathrm{opt}} = \frac{\Lambda}{4\pi\kappa} \tag{7}$$

where κ is the extinction coefficient of the inner body material (copper), with a value of approximately 6.9 at a wavelength of $\Lambda = 1064$ nm. The estimated optical skin depth for a single pulse was $\delta_{\mathrm{opt}} = 12.3$ nm, and the accumulated depth after 29 pulses was estimated to be $\delta_{\mathrm{opt}} = 356$ nm. Next, the theoretical melt depth, δ_{melt}, was estimated based on the energy conservation:

$$\delta_{\mathrm{melt}} = \frac{\eta E_{\mathrm{in}} / \left(\frac{\pi d}{4}\right)^2}{\rho_{\mathrm{IB}} \left\{ c_p \left(T_{\mathrm{m}} - T_{\mathrm{bg}} \right) + q_{\mathrm{m}} \right\}} \tag{8}$$

where η is the laser energy absorption coefficient of copper, with a value of 0.04 at a wavelength of 1070 nm (Baumann et al. 2021), d is the focused beam diameter, which was approximated by the measured diameter of the ablation mark because the actual beam diameter at the focal point was not measured, ρ_{IB}, c_p, T_{m}, and q_{m} are the density, isobaric specific heat, melting point, and latent heat of fusion of copper, respectively, and T_{bg} is the background temperature. The estimated theoretical melt depth for a single laser pulse was

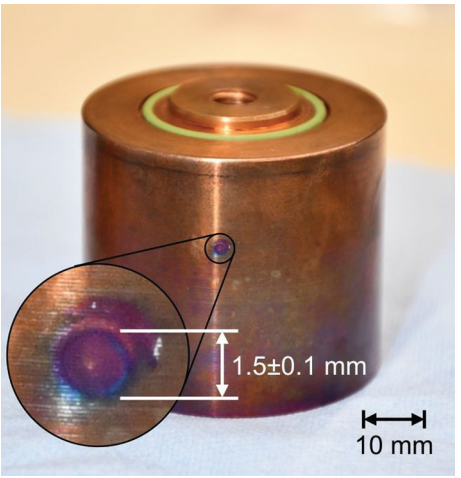


Figure 2. Side view of the inner body completing 29 test cases together with an enlarged view of the laser ablation mark (bottom left).

$\delta_{melt} = 139$ nm, and the accumulated depth after 29 pulses was estimated to be $\delta_{melt} = 4.0$ μm. Finally, the thermal diffusion length, δ_{th}, was estimated as:

$$\delta_{th} = \sqrt{\alpha \Delta t_{FWHM}} \tag{9}$$

where α is the thermal diffusivity of copper. The estimated thermal diffusion length for a single laser pulse was $\delta_{th} = 539$ nm, and the accumulated length after 29 pulses was estimated to be $\delta_{th} = 15.6$ μm.

The estimated characteristic depth scales associated with the laser ablation process were on the order of nanometers for a single pulse and in the nanometer-to-micrometer range after the test campaign, which is consistent with the value reported by Börner (2022). These results suggest that the laser ignition process does not cause significant structural degradation of either the optical components or the inner body material under repeated operation.

Flowfield history in exemplary cases

The evolutions of the compensated mass flow rates, plenum pressures, and chamber pressure in two cases with different laser trigger timingsare shown in Figure 3. In both cases, a first spike in the mass flow rate and plenum pressure was observed approximately 100 ms after the run-valve open signal was issued. The laser trigger signal was then issued after the prescribed delay, resulting in a second spike in the mass flow rates, plenum pressures, and chamber pressure. Despite the difference in laser trigger timing, the flow variables reached a quasi-steady state from $t = 150$ ms until the run-valve closure signal was issued. This plateau region, highlighted in gray, was defined as the "steady state," and the mean temperature and pressure values in this region were used in the subsequent analyses. Finally, fluctuations in the mass flow rates, plenum pressures, and chamber pressure were observed approximately 200 ms after the run-valve closure signal, marking the transition to the shutdown phase.

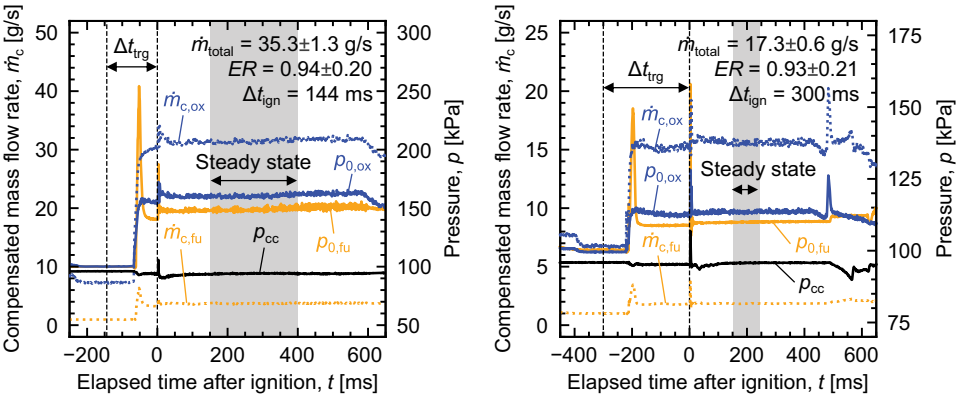


Figure 3. Time histories of compensated mass flow rates and pressures for $\dot{m}_{total} = 35.3 \pm 1.3$ g/s and $ER = 0.94 \pm 0.20$ (left) and for $\dot{m}_{total} = 17.3 \pm 0.6$ g/s and $ER = 0.93 \pm 0.21$ (right). The dotted lines denote the compensated mass flow rates, whereas the solid lines denote the pressures. The fuel-related quantities are shown in orange, the oxidizer-related quantities in blue, and the chamber pressure in black.

Next, the pressure fluctuations measured by the piezo-electric pressure sensor and the chemiluminescence intensity fluctuations measured by the optical probe were analyzed using the short-time Fourier transform with a window length of 4.1 ms. Spectrograms of each signal were then generated based on power spectral density, as shown in Figures 4 and 5. In Figure 4 ($\dot{m}_{\text{total}} = 35.3 \pm 1.3$ g/s and $ER = 0.94 \pm 0.20$), a distinct dominant frequency component of $f = 18.8 \pm 1.0$ kHz was observed during the steady state in both spectrograms. This indicates the presence of a pressure-coupled combustion wave, which may either rotate or oscillate in the axial, azimuthal, or radial direction in the annular channel. To distinguish between these possibilities, the acoustic resonant frequencies in the axial, azimuthal, and radial directions were calculated using the following equations:

$$f_{\text{axial}} = \frac{(2n-1)a}{4\left(L+0.61\frac{D_{\text{mean}}}{2}\right)} \tag{10}$$

$$f_{\text{azm}} = \frac{na}{\pi D_{\text{mean}}} \tag{11}$$

$$f_{\text{rad}} = \frac{na}{D_{\text{out}}-D_{\text{in}}} \tag{12}$$

where n is the acoustic mode number, a is the sound speed of the burned gas, and L and D_{mean} are the length and mean diameter of the annular channel, respectively. Note that the radial resonant frequency was approximated by assuming a one-dimensional acoustic oscillation between two parallel plates separated by the annular channel width. The first-mode resonant frequencies were $f_{\text{axial}} = 4.7$ kHz, $f_{\text{azm}} = 8.3$ kHz, and $f_{\text{rad}} = 75.7$ kHz, respectively, and none of them matched the detected peak frequency, suggesting that the peak was not attributed to a simple acoustic resonance mode but rather to the rotating

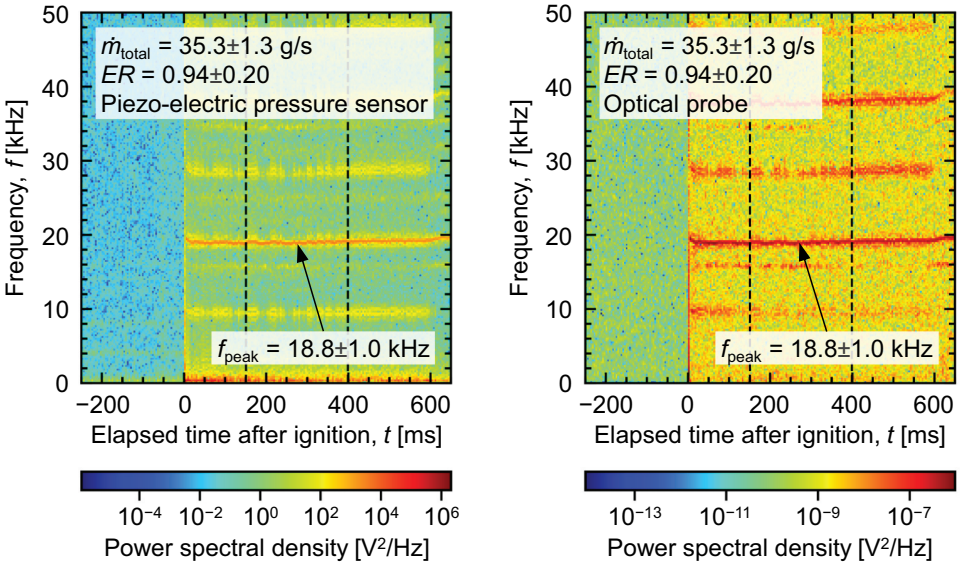


Figure 4. Chamber pressure spectrogram measured by the piezo-electric pressure sensor (left) and chemiluminescence intensity spectrogram measured by the optical probe (right) for $\dot{m}_{\text{total}} = 35.3 \pm 1.3$ g/s and $ER = 0.94 \pm 0.20$. The interval between the dashed lines denotes the steady state.

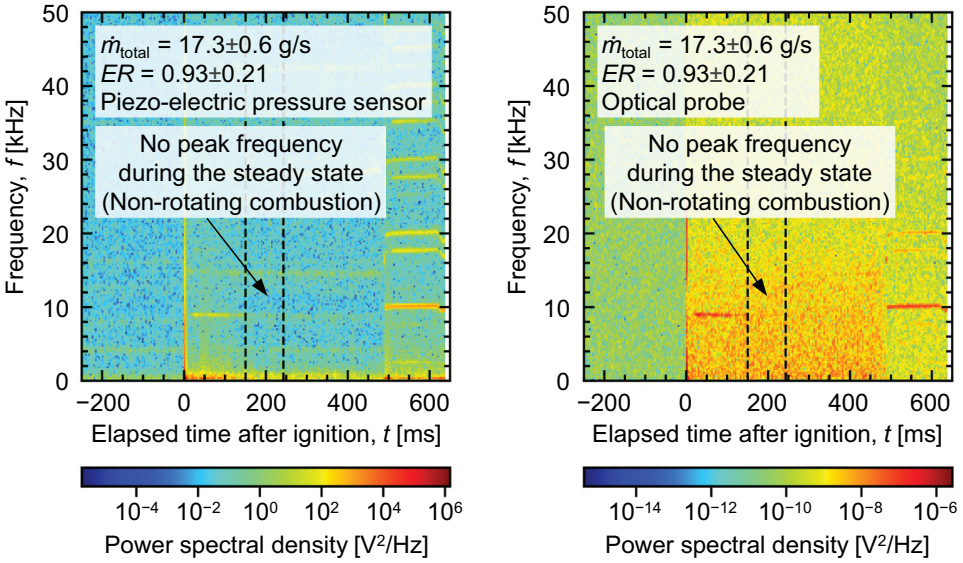


Figure 5. Chamber pressure spectrogram measured by the piezo-electric pressure sensor (left) and chemiluminescence intensity spectrogram measured by the optical probe (right) for at $\dot{m}_{total} = 17.3 \pm 0.6$ g/s and $ER = 0.93 \pm 0.21$. The interval between the dashed lines denotes the steady state.

combustion coupled with pressure waves. The corresponding peak frequency was then converted into the propagation velocity of the rotating chemiluminescence pattern in subsequent analyses to determine whether the rotating combustion wave corresponded to a detonation wave.

In contrast, no such peak was observed during the steady state in Figure 5 ($\dot{m}_{total} = 17.3 \pm 0.6$ g/s and $ER = 0.93 \pm 0.21$), indicating that neither rotating nor oscillating combustion wave was established in the channel. However, in this case, two comparatively weak peak frequency components at $f \approx 10$ kHz were observed at $t \approx 0$ ms and $t \approx 500$ ms. The former peak was more pronounced in the chemiluminescence spectrogram than in the pressure spectrogram, suggesting a combustion wave weakly coupled with pressure waves, either through rotation or oscillation. The second peak was clearly visible in both spectrograms, suggesting a more pronounced coupling between the combustion wave and pressure waves. Since $t \approx 500$ ms coincides with the onset of operating condition changes associated with run-valve closure, as shown in Figure 3 (right), this suggests that the change in operating conditions may have triggered this combustion mode. Although this behavior may be associated with transient quenching and re-initiation of rotating detonation waves, further investigation of this transient behavior requires spatiotemporal reconstruction of wave dynamics using synchronized high-frequency pressure measurements and high-speed imaging, which is beyond the scope of the present study.

The high-speed camera images were analyzed following the method proposed by Bennewitz et al. (2019). The evolutions of the number, N, and velocity, u, of the bright spots in the images representing chemiluminescence are shown in Figures 6 and 7. Hereafter, the clockwise rotation of the chemiluminescence pattern is abbreviated as CW, whereas the counterclockwise rotation is abbreviated as CCW. In Figure 6

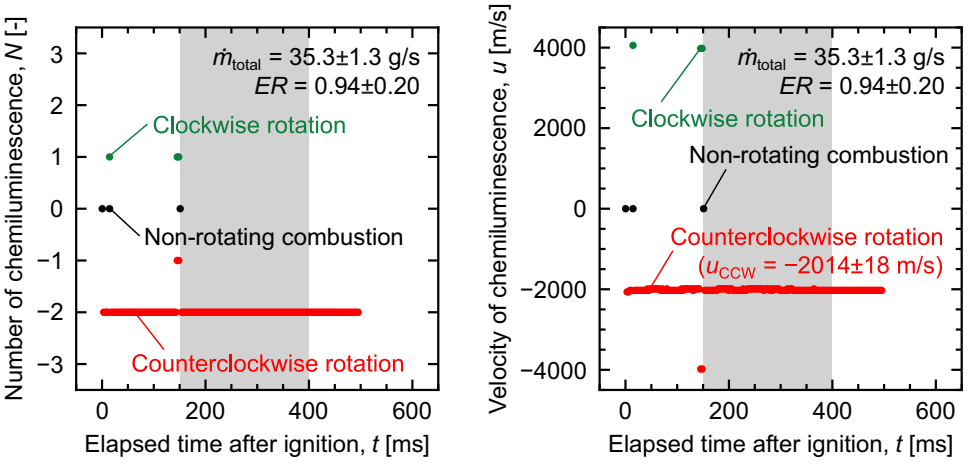


Figure 6. Time history of the number (left) and velocity (right) of the rotating chemiluminescence pattern for $\dot{m}_{total} = 35.3 \pm 1.3$ g/s and $ER = 0.94 \pm 0.20$. The green circles denote the clockwise rotation expressed by positive values, the red circles denote the counterclockwise rotation expressed by negative values, and the black circles denote the non-rotating combustion.

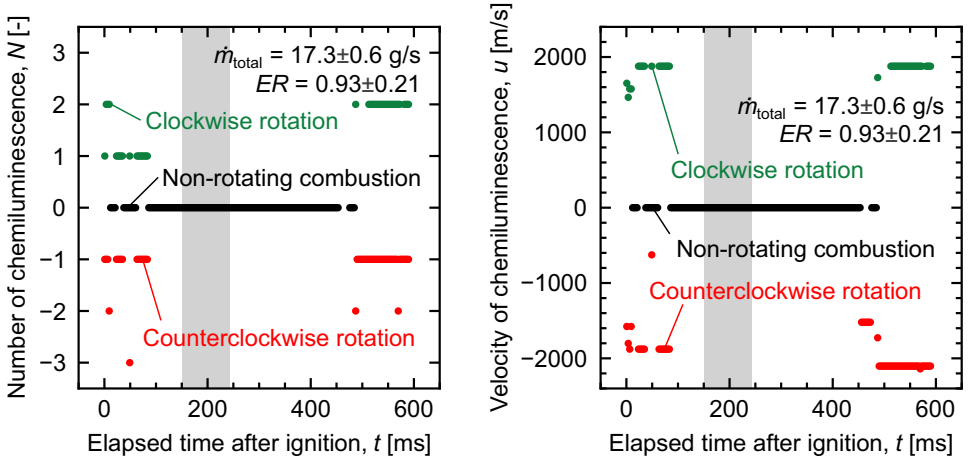


Figure 7. Time history of the number (left) and velocity (right) of the rotating chemiluminescence pattern for $\dot{m}_{total} = 17.3 \pm 0.6$ g/s and $ER = 0.93 \pm 0.21$. The green circles denote the clockwise rotation expressed by positive values, the red circles denote the counterclockwise rotation expressed by negative values, and the black circles denote the non-rotating combustion.

($\dot{m}_{total} = 35.3 \pm 1.3$ g/s and $ER = 0.94 \pm 0.20$), two combustion waves rotating in the counterclockwise direction with a propagation velocity of $u_{CCW} = -2014 \pm 18$ m/s were detected during the steady state. However, in Figure 7 ($\dot{m}_{total} = 17.3 \pm 0.6$ g/s and $ER = 0.93 \pm 0.21$), no rotating chemiluminescence pattern was detected. Here, the ratio of the duration of a specific rotational mode to the total duration of the steady state was defined as the "stability," σ. For example, in Figure 6, the stability of the clockwise rotation was $\sigma_{CW} = 0$, as no clockwise rotation was detected, whereas that of

the counterclockwise rotation was $\sigma_{CCW} = 0.99$. To determine whether the observed rotating chemiluminescence pattern corresponded to a detonation wave, the number, velocity, and stability were used in the following analyses.

Phenomenological description of the initial ignition process

Before assessing detonation propagation at the steady state, the initial ignition and flame development processes of the laser-ignited RDE were characterized by describing the flowfield evolution on microsecond and millisecond timescales.

First, the flowfield evolution on the microsecond timescale is discussed. The sequential images of chemiluminescence intensity for LAI and LSI under comparable operation conditions are presented in Figure 8. In the case of LAI at $\dot{m}_{total} = 35.3 \pm 1.3$ g/s and $ER = 0.94 \pm 0.20$, a laser ablation plasma was formed on the inner wall at $t = 5.6$ μs, which subsequently triggered the formation of an initial flame kernel at the same location at $t = 38.9$ μs. It was considered that, as reported by Takahashi and Kato (2021), the vortex ring induced by laser ablation collided with the inner wall, thereby enhancing the development of the flame kernel in the vicinity of the wall. At $t = 38.9$ μs, another flame kernel was formed near the outer wall due to the interaction with the ablation products. The initial and secondary flame kernels subsequently coalesced and developed into a channel-spanning combustion wave at $t = 117$ μs, which propagated along the inner wall. This propagation behavior was considered to be related to the suppression of boundary layer development near the outer wall, resulting from the injector arrangement near the outer wall and the radial deflection of the post-mixing jet flow. At $t = 133$ μs, two local explosions occurred simultaneously near the outer wall, leading to the formation of two counter-rotating overdriven detonation waves propagating at 3092 m/s. The first collision of these waves was observed at $t = 156$ μs. In the subsequent timeframes, the waves repeatedly collided with each other, and the chemiluminescence intensity associated with the waves gradually decreased.

In the case of LSI at $\dot{m}_{total} = 35.4 \pm 1.1$ g/s and $ER = 0.98 \pm 0.13$, a laser-induced spark plasma was formed at a radial position corresponding to $D = 50 - 58$ mm at $t = 5.6$ μs. In addition, a laser-induced ablation plasma was formed on the inner wall at $t = 11.1$ μs. According to Phuoc and White (2000), for an incident laser energy of 27 mJ, the energy transmission ratio was approximately 40% in hydrogen at 101.3 kPa and approximately 12% in oxygen at the same pressure. Therefore, the laser beam transmitted through the spark plasma was considered to have reached the inner wall and induced ablation. The initial flame kernels generated by these plasmas subsequently coalesced into a single flame kernel at $t = 38.9$ μs and developed into a combustion wave propagating along the inner wall at $t = 117$ μs. At this point, the size and propagation velocity of the combustion wave were comparable to those observed in the LAI case at $t = 117$ μs, indicating that the influence of the ignition method was limited to the initial stage on the order of 1–100 μs. After $t = 117$ μs, the propagation behavior of the combustion wave became similar to that observed in the LAI case. At $t = 144$ and 150 μs, two local explosions occurred near the outer wall, forming two overdriven detonation waves. Similar to the LAI case, these detonation waves repeatedly collided with each other, accompanied by a gradual decrease in chemiluminescence intensity.

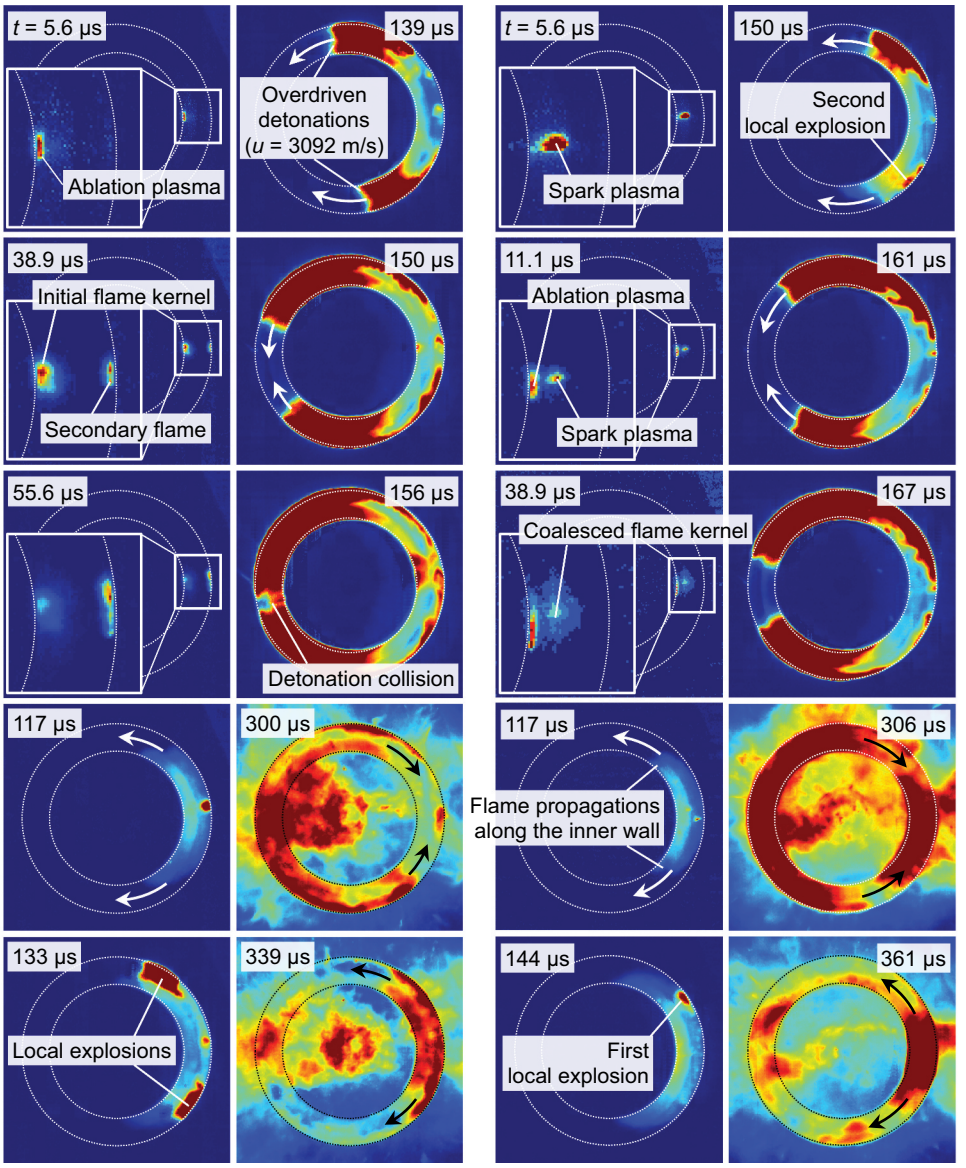


Figure 8. Sequential images of the spatial distribution of chemiluminescence intensity recorded by the high-speed camera for LAI at $\dot{m}_{total} = 35.3 \pm 1.3$ g/s and $ER = 0.94 \pm 0.20$ (left) and LSI at $\dot{m}_{total} = 35.4 \pm 1.1$ g/s and $ER = 0.98 \pm 0.13$ (right). The number described in each image represents the elapsed time after laser emission. The light intensity was normalized independently for each image to clearly visualize the contour of the combustion wave.

Comparing the flame kernel development and combustion wave propagation between LAI and LSI, the ignition success and detonation onset timing were found to be comparable despite the differences in the initial flame kernel morphologies. Specifically, LAI produced two hemispherical flame kernels on the inner and outer walls, whereas LSI produced a relatively large spherical flame kernel near the channel

center and a relatively small hemispherical flame kernel on the inner wall. Despite these differences, the flame kernels developed into a channel-spanning combustion wave by $t = 117$ μs, suggesting that the overall flame kernel development process was comparable between the two ignition methods. In addition, although the axial dimension of the initial flame kernels was not measured in the present study, flame acceleration is generally governed by a positive feedback loop involving increases in flame surface area, burning velocity, and heat release rate, accompanied by the generation of compression waves. Therefore, it was inferred that the initial flame kernels likely had comparable effective flame surface areas despite their different morphologies, resulting in the limited influence of the ignition method on the ignition success rate. Furthermore, once a self-sustained combustion wave had formed, the subsequent deflagration-to-detonation transition is expected to be governed primarily by the positive feedback loop of flame acceleration and the flow conditions ahead of the combustion wave, rather than by the initial flame kernel morphology. Because the combustion wave morphology became comparable after $t = 117$ μs under the similar flow conditions, the detonation onset timing was also similar between LAI and LSI.

Next, based on high-speed camera images, the azimuthal wave diagram at the mean channel diameter $D_{\mathrm{mean}} = 58$ mm was generated in the case of LAI at $\dot{m}_{\mathrm{total}} = 35.3 \pm 1.3$ g/s and $ER = 0.94 \pm 0.20$, as shown in Figure 9. In the figure, a typical deflagration-to-detonation transition was observed, followed by the formation of two counter-rotating overdriven detonation waves propagating at 3092 m/s and the development of their induced flow fields. These waves collided with each other and gradually decayed, becoming barely observable in the wave diagram after $t = 0.65$ ms. As a possible explanation for this decay, Hou et al. (2026) reported the effect of detonation wave collisions: when a wave collision occurs, it creates a high-pressure region behind the colliding detonation waves, which suppresses fresh reactant injections. When such collisions occur repeatedly, the fill height of fresh reactants gradually decreases, potentially leading to temporary quenching, as observed in the present study. Given that the two colliding detonation waves observed before $t = 0.65$ ms were in an overdriven state, the influence of the high-pressure burned gas region was considered to be greater than that in a typical rotating detonation wave. Therefore, the overdriven detonation waves were considered to decay rapidly after their formation by the local explosions.

After the decay period of $t = 0.65 - 1.2$ ms, multiple detonation waves appeared, consisting of four clockwise-propagating waves and four counterclockwise-propagating waves at 1665 m/s. This behavior was considered to represent as a reinitiation phenomenon. According to Jo et al. (2026), when a detonation wave can no longer sustain its structure, it transitions to deflagration. However, because this localized and non-uniform deflagration induces a pressure difference within the engine, a detonation wave can be reinitiated once the pressure difference becomes sufficiently large. Therefore, the interval of $t = 0.65 - 1.2$ ms was considered to represent the time required for the pressure difference to build up.

The number of waves, propagation velocity, and chemiluminescence intensity of the reinitiated detonation waves gradually decreased until $t = 3.1$ ms, at which point two stably rotating detonations propagating at 2022 m/s were observed. As confirmed in Figure 6, these wases continued to propagate for the remainder of the test without significant changes in their number or propagation velocity.

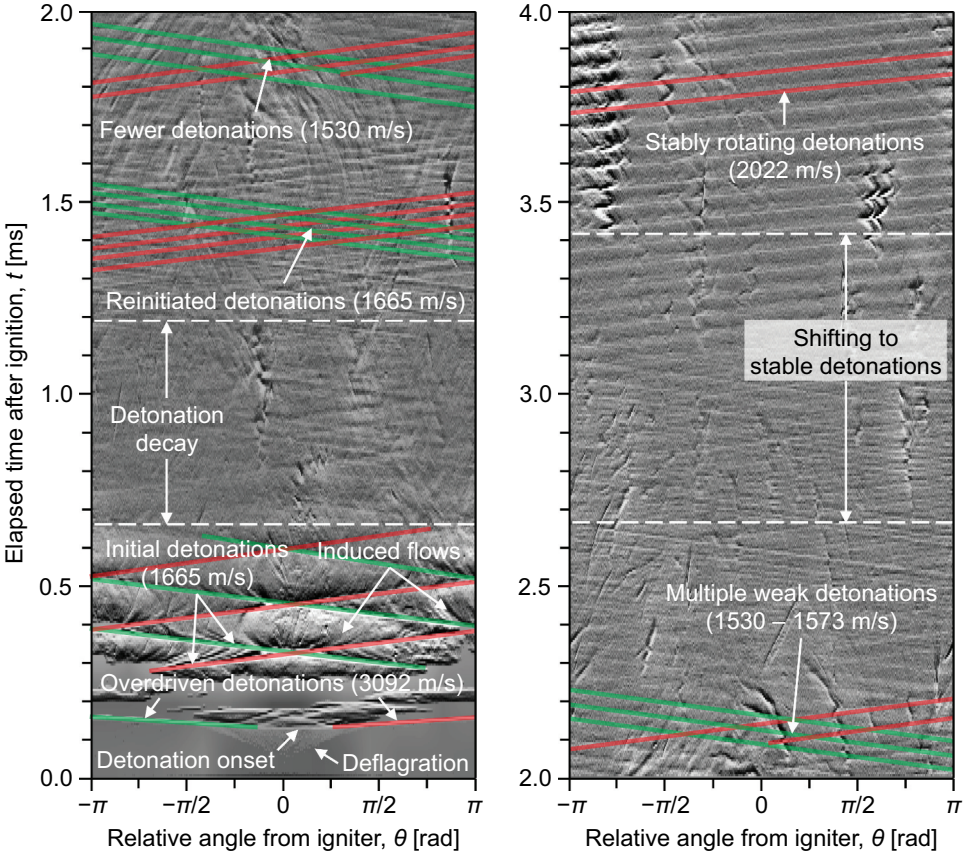


Figure 9. Azimuthal wave diagram at the mean channel diameter of $D_{mean} = 58$ mm for LAI at $\dot{m}_{total} = 35.3 \pm 1.3$ g/s and $ER = 0.94 \pm 0.20$. The original images were processed using differential imaging so that zero light intensity change corresponded to the mid-gray pixel value and moving objects were visualized as deviations from this value. The green lines indicate waves rotating in the clockwise direction, and the red lines indicate waves rotating in the counterclockwise direction.

Based on Figures 8 and 9, the sequence of the initial process in the laser-ignited RDE and the corresponding timescales are summarized in Table 2. First, on the order of 1 μs, an ablation or breakdown plasma was generated. The plasma then generated initial flame kernels on the order of 10 μs, which subsequently developed into a deflagration on the order of 10–100 μs. By comparing the flowfields between LAI and LSI, it was found that the influence of the ignition method was reflected in the flowfield only up to this timescale. After this stage, the deflagrations gradually accelerated, and local explosions occurred on the order of 100 μs. The deflagrations transitioned into overdriven detonation waves, and multiple wave collisions occurred, resulting in the gradual decay of these overdriven detonation waves on a timescale of 100 μs – 1 ms. On the order of 1 ms, multiple detonation waves were reinitiated, and their number and propagation velocity became adjusted until stably rotating detonation waves were established. Given that wave collisions occur during both the decay process of the overdriven detonation waves and the adjustment process of the

Table 2. Sequence of the initial process in the laser-ignited RDE and the corresponding timescales.

Order of time	Description of the stage
O (1 ns)	Laser irradiation
O (1 μs)	Ablation/breakdown plasma generation
O (10 μs)	Initial flame kernels formation
O (10–100 μs)	Initial deflagration
O (100 μs)	Local explosion and overdriven detonation onset
O (100 μs − 1 ms)	Decay of overdriven detonation
O (1 ms)	Reinitiation of multiple detonations and adjustment of wave number and propagation velocity
O (>1 ms)	Stably rotating detonations

reinitiated detonation waves, the characteristic timescales of the final three stages in Table 2 are expected to depend on both the operating condition and the chamber dimensions.

Assessment of detonation propagation based on non-dimensional propagation velocity

The propagation of rotating detonation waves during the steady state was assessed in this section. The assessment was conducted using two indicators: the non-dimensional propagation velocity of the rotating chemiluminescence pattern and the non-dimensional maximum fill height of the unburned gas ahead of the combustion wave.

First, the mean velocity of the rotating chemiluminescence pattern during the steady state, u, was normalized by the Chapman-Jouguet (CJ) detonation speed, u_{CJ}. The CJ detonation speed was calculated using the Shock and Detonation Toolbox (Explosion Dynamics Laboratory 2023) and Cantera (Goodwin et al. 2023) with the detailed chemical kinetic mechanism proposed by Burke et al. (2011). Figure 10 presents the results of three-times repeated tests performed under the same operating condition.

In Figure 10, the chemiluminescence at the lowest mass flow rates, $\dot{m}_{total}$ = 17.7 and 17.1 g/s, exhibited three distinct modes: no rotation (the third trial in both LAI and LSI), rotation at the burned-gas sound speed with high stability ($\sigma \approx 1.0$; the first and second trial in LAI), and rotation at a velocity slightly higher than the burned-gas sound speed with low stability ($\sigma < 0.5$; the first and second trial in LSI). Note that the black circles in Figure 10 denote the burned-gas sound speed, a, calculated using Cantera (Goodwin et al. 2023). As explained below, these three modes can be interpreted as non-rotating isobaric combustion, rotating combustion loosely coupled with pressure waves, and a transitional combustion mode between the two, respectively.

Regarding the first mode, no pronounced peak frequency was observed during the steady state in either the pressure or chemiluminescence spectrogram, as shown in Figure 5. Therefore, similar to a conventional rocket combustor, the propellants were considered to burn and be exhausted directly from the chamber without forming any rotating or oscillating combustion mode.

To examine the second mode in greater detail, the raw outputs of the piezo-electric pressure sensor and the optical probe in the case of LAI at $\dot{m}_{total} = 17.6 \pm 0.5$ g/s, $ER = 0.95 \pm 0.21$ are shown in Figure 11. Note that, because the pressure sensor gradually accumulated electric polarization in its internal quartz piezoelectric crystal, as reported by Lin et al.

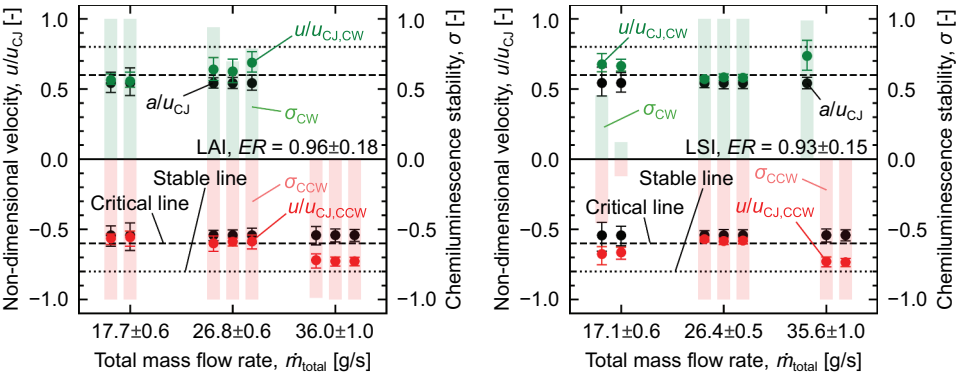


Figure 10. Comparison of non-dimensional propagation velocity and stability of the rotating chemiluminescence pattern in the three-times repeated tests in LAI (left) and LSI (right). The green and red circles are the non-dimensional propagation velocity of the rotating chemiluminescence pattern in the clockwise and counterclockwise direction, respectively. The black circles are the non-dimensional sound speed of the burned gas. The dashed line is the critical threshold (60% CJ speed), and the dotted line is the stable threshold (80% CJ speed). The green and red bar charts are the stability of the rotating chemiluminescence pattern in the clockwise and counterclockwise direction, respectively. The absence of circles and bar charts, e.g. the clockwise and counterclockwise rotations in the third trial of $\dot{m}_{total}$ = 17.7 g/s in LAI and the clockwise rotation in the second and third trials of $\dot{m}_{total}$ = 35.6 g/s in LSI, indicates that no rotating chemiluminescence pattern was observed in the corresponding direction.

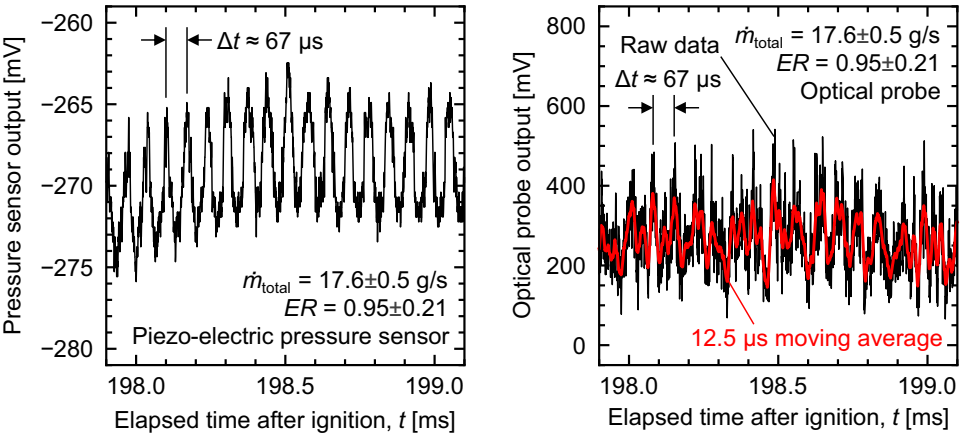


Figure 11. Raw outputs of the piezo-electric pressure sensor (left) and the optical probe (right) for LAI at $\dot{m}_{total} = 17.6 \pm 0.5$ g/s and $ER = 0.95 \pm 0.21$, corresponding to the first trial at the lowest mass flow rate shown in Figure 10 (left).

(2015), its output did not represent the absolute pressure. Therefore, the raw pressure signal is presented in units of voltage in the present study. As shown in Figure 11, both the pressure and light intensity signals exhibited periodic fluctuations with a period of approximately 67 μs. However, the waveforms were sinusoidal rather than shock-like, indicating that the combustion wave was coupled with a pressure wave rather than shock waves. Given that the propagation velocity of the rotating chemiluminescence pattern was nearly equal to

the burned-gas sound speed, as shown in Figure 10, this combustion mode was interpreted as a rotating combustion wave loosely coupled with pressure waves.

Regarding the third mode, a distinct transition in the combustion mode was observed. Figure 12 shows the time history of propagation velocity of the rotating chemiluminescence pattern and an enlarged view of the raw output of the piezo-electric pressure sensor. As shown in Figure 12 (left), during the period from $t = 150$ to 210 ms, clockwise- and counterclockwise-rotating chemiluminescence patterns propagated at velocities of 1802 and −1802 m/s, respectively. The corresponding pressure waveform was sinusoidal and rather than shock-like, as shown in Figure 12 (right), similar to that observed for the second combustion mode. However, after $t \approx 211.5$ ms, the pressure fluctuation gradually decayed, and the regular waveform changed into a noise-like signal. This timing coincided with the disappearance of both the clockwise and counterclockwise rotating chemiluminescence patterns and the onset of non-rotating combustion, as shown in Figure 12 (left). Given that the second mode was interpreted as a combustion wave loosely coupled with pressure waves, these observations suggest that the coupling could not be sustained throughout the steady state in this case. Therefore, the third combustion mode can be interpreted as a transitional mode between the first and second modes because the coupling between the combustion wave and the pressure wave was intermittently established and lost.

At the intermediate mass flow rates of $\dot{m}_{\mathrm{total}} = 26.8$ and 26.4 g/s in Figure 10, although the stability and repeatability were higher than those at the lowest mass flow rates, the non-dimensional propagation velocity of the rotating chemiluminescence pattern was $u/u_{\mathrm{CJ}} \approx \pm 0.6$, which was still close to the burned-gas sound speed. As shown in Figure 13, both the pressure and light intensity signals exhibited periodic fluctuations with a period of approximately 57 μs, similar to those observed for the second combustion mode at the lowest mass flow rate (Figure 11). However, the pressure waveform also exhibited an envelope with a period of approximately 308 μs, corresponding to an oscillation frequency of 3.2 kHz. Since this frequency was comparable to the previously calculated axial resonant frequency of $f_{\mathrm{axial}} = 4.7$ kHz, it was inferred that the combustion wave, which was loosely coupled with

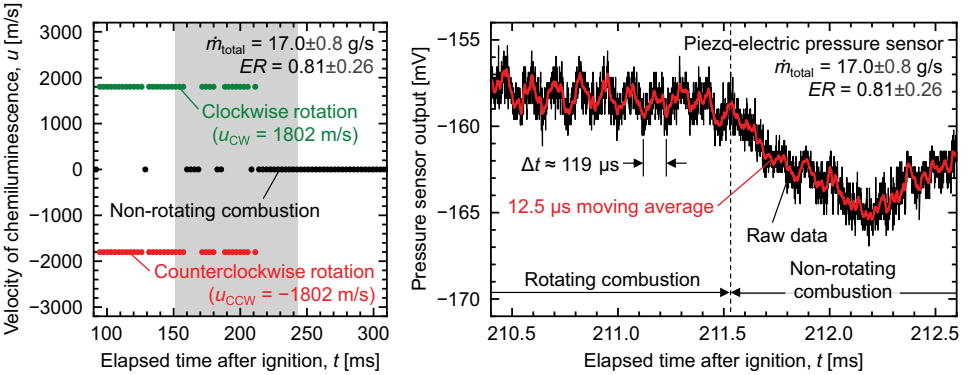


Figure 12. Time history of the propagation velocity of the rotating chemiluminescence pattern (left) and an enlarged view of the raw output of the piezo-electric pressure sensor during the combustion mode transition (right) for LSI at $\dot{m}_{\mathrm{total}} = 17.0 \pm 0.8$ g/s and $ER = 0.81 \pm 0.26$, corresponding to the first trial at the lowest mass flow rate shown in Figure 10 (right).

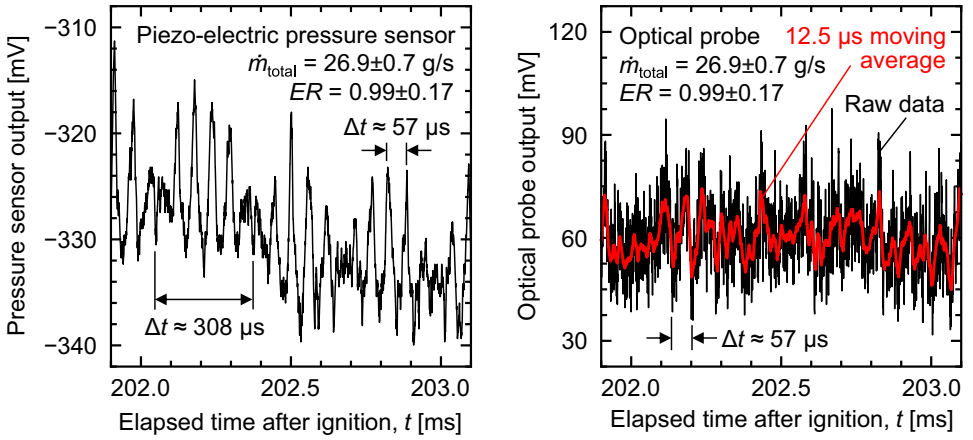


Figure 13. Raw outputs of the piezo-electric pressure sensor (left) and the optical probe (right) for LAI at $\dot{m}_{total} = 26.9 \pm 0.7$ g/s and $ER = 0.99 \pm 0.17$, corresponding to the third trial of the intermediate mass flow rate shown in Figure 10 (left).

pressure waves, was additionally coupled with the axial acoustic mode of the combustion chamber at the intermediate mass flow rates.

At the highest mass flow rates of $\dot{m}_{total} = 36.0$ and 35.6 g/s in Figure 10, the non-dimensional propagation velocity of the rotating chemiluminescence pattern was $u/u_{CJ} \approx \pm 0.75$ in a single direction. As shown in Figure 14, both the pressure and optical probe signals exhibited repeated spikes with a period of approximately 53 μs. In particular, the pressure waveform resembled that of a typical detonation wave. However, because the sensing diaphragm of the piezo-electric pressure sensor was approximately 5.6 mm in diameter, which was relatively large compared with the spatial scale of the detonation front, an abrupt pressure rise associated with the passing detonation wave was not resolved in the pressure signal. The optical probe signal exhibited higher and more distinct spikes

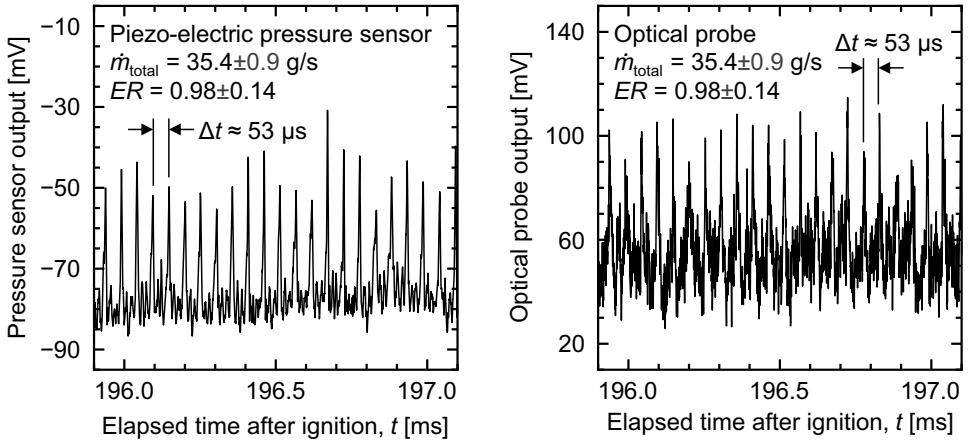


Figure 14. Raw outputs of the piezo-electric pressure sensor (left) and the optical probe (right) for LSI at $\dot{m}_{total} = 35.4 \pm 0.9$ g/s and $ER = 0.98 \pm 0.14$, corresponding to the second trial of the highest mass flow rate shown in Figure 10 (right).

than those observed at the lowest and intermediate mass flow rates, indicating that the combustion was more intense and that the light-emitting region within the combustion wave more localized in the azimuthal direction. Based on the observations shown in Figures 10 and 14, it was indicated that a rotating detonation wave propagated in a single direction at the highest mass flow rates.

Since the absolute pressure was not measurable by the piezo-electric pressure sensor in the present study, the first assessment of detonation propagation was carried out based on the non-dimensional propagation velocity of the rotating chemiluminescence pattern. As evaluation criteria, the studies by Kudo et al. (2011) and Liu et al. (2018) were referenced. In the study by Kudo et al. (2011), an oblique detonation wave propagated through a rectangular bent tube, and three propagation regimes were defined based on the wave velocity: a stable regime for $u \geq 0.8u_{CJ}$, a critical regime for $0.6u_{CJ} \leq u < 0.8u_{CJ}$, and an unstable regime for $u < 0.6u_{CJ}$. Liu et al. (2018) theoretically investigated the deflagration-to-detonation transition and likewise regarded 60% of the CJ detonation speed as the critical condition, since it corresponds to maximum propagating velocity of a deflagration and is nearly equal to the burned-gas sound speed. Although Kudo et al. (2011) investigated an ethylene-oxygen mixture, whereas Liu et al. (2018) considered methane-oxygen and ethylene-air mixtures, both studies consistently identified 60% of the CJ detonation speed as the critical threshold. Although wall friction and channel curvature may affect the absolute propagation velocity of rotating detonation waves, the threshold of $u/u_{CJ} = 0.6$ can be adopted as a first-order phenomenological criterion to distinguish detonation-like propagation from deflagration-like propagation. In addition, using the non-dimensional propagation velocity enables direct comparison among different propellant combinations and operating conditions with different CJ velocities in the future studies. Nevertheless, further validation using different combustor geometries and operating conditions will be necessary before establishing it as a universal criterion. Accordingly, based on these studies, 60% and 80% of the CJ detonation speed were plotted in Figure 10 as the critical and stable thresholds, respectively.

As shown in Figure 10, the criterion of $u/u_{CJ} > 0.6$ was satisfied only at the highest mass flow rates. As the mass flow rate decreased, the combustion mode gradually shifted toward non-rotating combustion, indicating that the coupling between the combustion wave and the pressure waves became increasingly difficult to sustain. In particular, the cases at $\dot{m}_{total} = 17.7$ and 17.1 g/s were considered to be located near the boundary beyond which the coupling could no longer be maintained, and therefore, small variations in the initial condition could alter the resulting combustion mode. Furthermore, because these trends were essentially identical for both LAI and LSI, the ignition method was considered to have only a minor influence on the establishment and stabilities of rotating detonations at the steady state.

As shown in Figure 15, the assessment of detonation propagation based on the non-dimensional propagation velocity of the rotating chemiluminescence pattern was also performed for different total mass flow rates and equivalence ratios in the LAI configuration. In Figure 15 (left), the non-dimensional velocity was $u/u_{CJ} \approx \pm 0.71$ at $\dot{m}_{total} = 32.1$ g/s and gradually decreased to $u/u_{CJ} = \pm 0.6$ as the mass flow rate increased. Nevertheless, as shown in Figure 16, the pressure and light intensity waveforms remained similar to those shown in Figure 14, indicating that detonation propagation was maintained even at higher mass flow rates. The decrease in the non-dimensional velocity observed in Figure 15 (left)

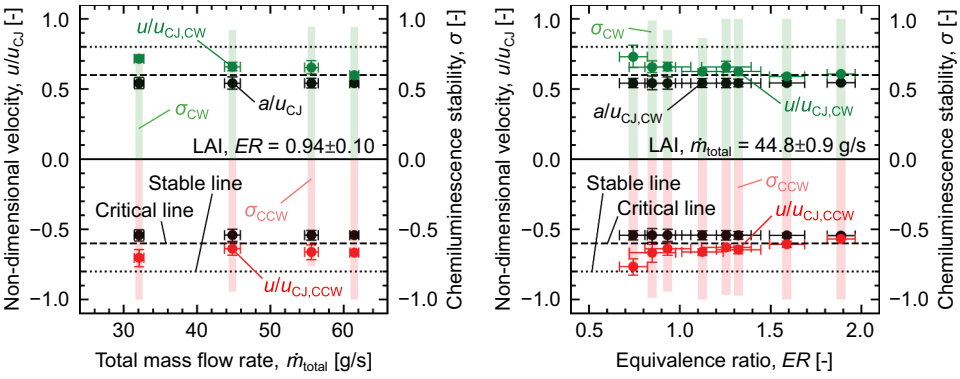


Figure 15. Comparison of non-dimensional propagation velocity and stability of the rotating chemiluminescence pattern as a function of the total mass flow rate (left) and equivalence ratio (right). The green and red circles are the non-dimensional propagation velocity of the rotating chemiluminescence pattern in the clockwise and counterclockwise direction, respectively. The black circles are the non-dimensional sound speed of the burned gas. The dashed line is the critical threshold (60% CJ speed), and the dotted line is the stable threshold (80% CJ speed). The green and red bar charts are the stability of the rotating chemiluminescence pattern in the clockwise and counterclockwise direction, respectively.

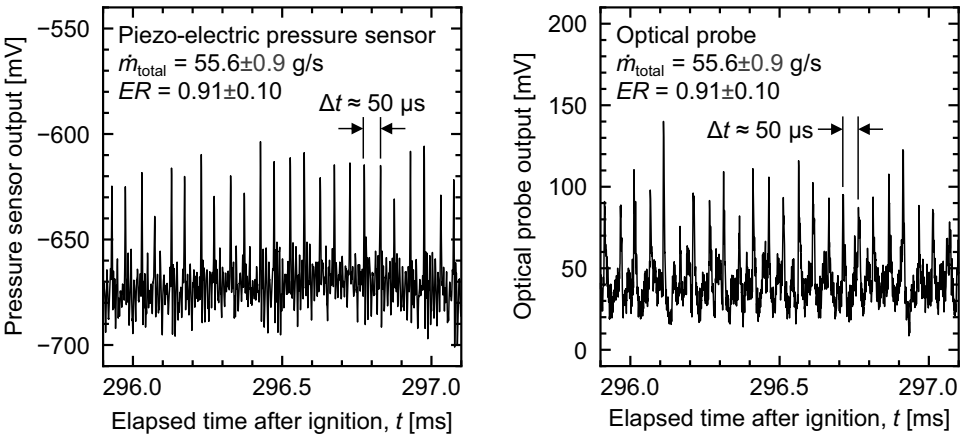


Figure 16. Raw outputs of the piezo-electric pressure sensor (left) and the optical probe (right) for LAI at $\dot{m}_{total} = 55.6 \pm 0.9$ g/s and $ER = 0.91 \pm 0.10$.

was considered to result primarily from the increase in the number of detonation waves. The total detonation wave number increased from 2 at $\dot{m}_{total} = 35.4 \pm 0.9$ g/s and $ER = 0.98 \pm 0.14$ to 10 at $\dot{m}_{total} = 61.5 \pm 0.6$ g/s and $ER = 0.99 \pm 0.06$. Although the relationship between the number of detonation waves and their propagation velocity has not yet been fully clarified, Koch et al. (2021) pointed out that an increase in the number of waves intensifies competition for the unburned gas, thereby modifying the wave spacing and the fill time of unburned gas, which consequently affects both the wave structure and propagation velocity. Therefore, the decrease in the non-dimensional velocity observed in Figure 15 (left) was considered to result from the insufficient supply of fresh propellants to each detonation wave due to the intensified competition among multiple waves.

In Figure 15 (right), the non-dimensional propagation velocity of the rotating chemiluminescence pattern decreased monotonically as the equivalence ratio increased and approached $u/u_{CJ} = 0.6$ in both rotational directions under fuel-rich conditions. A similar decrease on the fuel-rich side was reported by Wang and Wang (2015), who attributed the reduction in detonation propagation velocity to an increase in the specific heat ratio of the burned gas. In addition, because the detonation cell width and induction length increase as the mixture ratio deviates from the stoichiometric condition (Fickett and Davis 2000), it was considered that the coupling between the shock wave and the chemical reactions within the detonation wave could no longer be sustained for $ER > 1.5$. The increase in the non-dimensional velocity on the oxidizer-rich side can be explained by the injector arrangement and the resulting incomplete mixing, suggesting that the local mixture remained fuel-rich despite the global oxidizer-rich condition.

As shown in Figures 10 and 15, a prominent deficit in the non-dimensional propagation velocity was observed. In addition to the general deviation from the ideal CJ detonation velocity observed in conventional RDEs due to non-ideal effects such as wall friction and channel curvature, which can lead to incomplete energy release compared with the ideal CJ state, the aforementioned injector arrangement and the resulting incomplete mixing were considered to be major contributions to this velocity deficit. The injector plate used in the present study was originally manufactured for a thinner annular channel with an outer diameter of 68 mm and an inner diameter of 59 mm, in which the fuel and oxidizer jets were designed to impinge near the channel center. However, in the present study, the inner diameter was reduced to 48 mm, causing the jet impingement point shifted relatively to the outer wall. This suggests that the fresh propellant distribution became non-uniform, with the unburned gas concentrated near the outer wall while the burned gas remained near the inner wall. As suggested by Hou et al. (2026), the coexistence of burned and unburned gases can induce premature autoignition of the fresh reactants, thereby reducing the amount of propellant available to sustain rotating detonation waves and consequently leading to a velocity deficit.

Assessment of detonation propagation based on non-dimensional fill height

As the second indicator to assess detonation propagation, the maximum fill height of the unburned gas ahead of the combustion wave was estimated as follows. First, the velocity of the unburned-gas jet and its angle were calculated from the conservation of mass and momentum, as illustrated in Figure 17.

In Figure 17, U denotes the jet velocity, and θ denotes the jet angle with respect to the r-axis, which is equal to the injector-hole angle. The subscripts fu, ox, and fill denote the fuel, oxidizer, and unburned-gas jets, respectively. Here, the momentum conservation per unit time in the z- and r-directions are expressed as follows:

$$\dot{m}_{\mathrm{fill}} U_{\mathrm{fill}} \sin\theta_{fill} = \dot{m}_{\mathrm{fu}} U_{\mathrm{fu}} \sin\theta_{\mathrm{fu}} + \dot{m}_{\mathrm{ox}} U_{\mathrm{ox}} \sin\theta_{\mathrm{ox}} \tag{13}$$

$$\dot{m}_{\mathrm{fill}} U_{\mathrm{fill}} \cos\theta_{fill} = \dot{m}_{\mathrm{fu}} U_{\mathrm{fu}} \cos\theta_{\mathrm{fu}} + \dot{m}_{\mathrm{ox}} U_{\mathrm{ox}} \cos\theta_{\mathrm{ox}} \tag{14}$$

On the other hand, the mass conservation per unit time is expressed as follows:

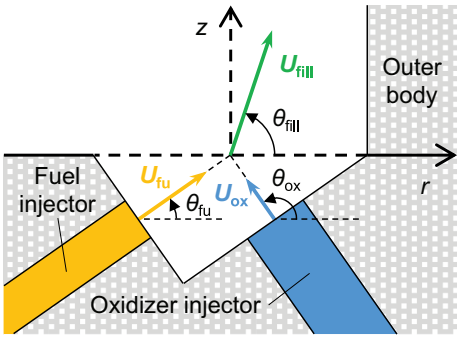


Figure 17. Enlarged cross-sectional view of a pair of injectors. The hole injector located at the lower left supplied the fuel jet (vector in orange), and the other hole injector located at the lower right supplied the oxidizer jet (vector in blue). Collision of the two jets occurred at the radial plane of $z = 0$, and the unburned gas mixture (vector in green) penetrated into the combustion chamber. The inclination angle of each jet was defined from the *r*-axis.

$$\dot{m}_{\mathrm{fill}} = \dot{m}_{\mathrm{fu}} + \dot{m}_{\mathrm{ox}} \tag{15}$$

The fuel and oxidizer jet velocities, U_{fu} and U_{ox}, were calculated from the isentropic flow equations using the mean plenum temperature, mean plenum pressure, and mean chamber pressure during the steady state:

$$U = \sqrt{\frac{2\gamma RT_0}{\gamma+1}} \tag{16}$$

$$U = \sqrt{\frac{2\gamma RT_0}{\gamma-1}\left\{1 - \left(\frac{p_{\mathrm{cc}}}{p_0}\right)^{\frac{\gamma-1}{\gamma}}\right\}} \tag{17}$$

Similar to Eqs. (4)–(6), Eq. (16) was used when the chamber-to-plenum pressure ratio was below the critical value, corresponding to sonic injection.

From Eqs. (13)–(17), the unburned-gas jet velocity, U_{fill}, and the jet angle, θ_{fill}, were calculated. These quantities were then used to estimate the maximum fill height of the unburned gas, h, using the following equation:

$$h = U_{\mathrm{fill}} \sin\theta_{\mathrm{fill}} \Delta t_{\mathrm{fill}} \tag{18}$$

where Δt_{fill} denotes the unburned-gas fill time, defined as the time interval between two successive detonation waves. The fill time was calculated using two methods: (1) the peak frequencies obtained from the pressure and chemiluminescence spectrograms and (2) the number of rotating waves and their propagation velocities obtained from high-speed camera images. In the former method, the fill time was calculated as follows:

$$\Delta t_{\mathrm{fill}} = \frac{1}{f_{\mathrm{peak}}} \tag{19}$$

When two distinct peak frequencies were observed in the spectrogram, each peak was considered to correspond to either clockwise or counterclockwise rotating waves. Therefore, instead of Eq. (19), the following equation was used:

$$\Delta t_{\mathrm{fill}} = \frac{1}{f_{\mathrm{peak},1} + f_{\mathrm{peak},2}} \tag{20}$$

The fill time was also calculated using the number of rotating waves and their propagation velocities obtained from the high-speed camera images:

$$\Delta t_{\mathrm{fill}} = \frac{\pi D_{\mathrm{out}}}{N_{\mathrm{CW}} u_{\mathrm{CW}} + N_{\mathrm{CCW}} u_{\mathrm{CCW}}} \tag{21}$$

As shown by these equations, Eqs. (20) and (21) are essentially identical but describe the detonation propagation from different perspectives. By substituting Eqs. (19)–(21) into Eq. (18), the maximum fill height was calculated.

The calculated fill height was subsequently normalized by the detonation cell width of the H_2–O_2 mixture, λ, following previous studies (Bykovskii et al. 2006; Weber et al. 2025). These studies assumed that rotating detonation waves can propagate as long as a sufficient amount of propellant is supplied ahead of the detonation wave and that the height of unburned-gas layer is correlated with the detonation cell width. For near-stoichiometric conditions, the cell size was estimated as a function of pressure using linear interpolation on a log-log scale based on the data points at $T = 293$ K and $ER = 1$ (Denisov and Troshin 1960; Voitsekhovskii et al. 1966; Strehlow 1969; Manzhalei et al. 1974; Lee and Matsui 1977; Knystautas et al. 1982; Desbordes 1990; Zitoun et al. 1995), which are available in the Detonation Database (Kaneshige and Shepherd 1997). For off-stoichiometric conditions, because cell size data were not available in the Detonation Database (Kaneshige and Shepherd 1997), the cell size was estimated based on the cell width data of H_2–air mixtures at various equivalence ratios (Guirao et al. 1982) and nitrogen dilution conditions (Knystautas et al. 1982; Kaneshige 1999), following the method proposed by Connolly-Boutin et al. (2021).

The calculated non-dimensional maximum fill height was compared with the empirical operational range of RDE, $h/\lambda = 12 \pm 5$ (Bykovskii et al. 2006), and the empirical threshold for high-probability detonation sustainment, $h/\lambda = 3$ (Weber et al. 2025). It should be noted that these empirical criteria are not universal ones for detonation propagation in RDEs. Previous studies have reported different critical values (Anand et al. 2016; Rankin et al. 2016), suggesting that the fill height can depend on the combustor geometry, injector configuration, mixture composition, and the resulting flow conditions. Moreover, because the experimental conditions in these previous studies differ from those of the present study, the applicability of their reported thresholds to the present RDE cannot be assumed. Since no generally accepted critical value of the non-dimensional fill height has been established under the current state of knowledge, $h/\lambda = 12 \pm 5$ and $h/\lambda = 3$ were used as empirical reference values, rather than as definitive criteria, for assessing detonation propagation in the present study. Systematic experiments using different combustor geometries, injector configurations, and mixtures would be necessary to establish the generalizability and applicability of such empirical criteria, which is beyond the scope of the present study.

In Figure 18, it was found that the non-dimensional fill heights obtained from different measurement methods were comparable, indicating the consistency of the sensors and measurement methods used in this experiment. In addition, the non-dimensional fill height decreased at higher total mass flow rates and higher equivalence ratios. Based on Eq. (21) and the decrease in the non-dimensional propagation velocity shown in Figure 15, it was inferred that the increase in the total number of detonation waves had a greater influence

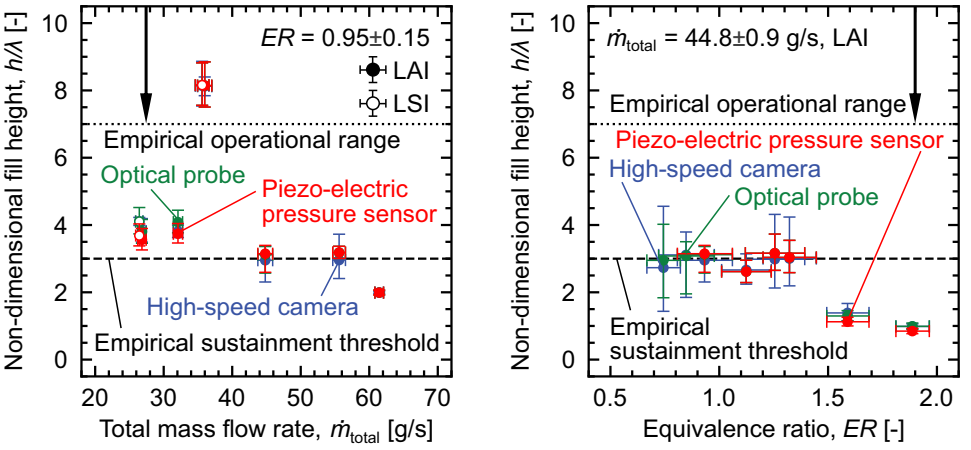


Figure 18. Comparison of the non-dimensional maximum fill height of unburned gas against the total mass flow rate (left) and the equivalence ratio (right). The closed and open circles denote LAI and LSI, respectively, and the color of circles denotes the measurement method: red for piezo-electric pressure sensor, green for optical probe, and blue for high-speed camera. The dotted line represents the lower limit of the empirical operational range of RDEs, $h/\lambda = 12 \pm 5$, reported by Bykovskii et al. (2006), and the dashed line at $h/\lambda = 3$ represents the empirical threshold for high-probability detonation sustainment reported by Weber et al. (2025). Note that those cases with lower repeatability were not plotted in the figure. In addition, because the piezo-electric pressure sensor failed during the tests at $ER = 0.74$ and 0.85, the corresponding plots were not displayed in the figure (right).

than the decrease in propagation velocity on the reduction of the non-dimensional fill height. For example, in the cases of $\dot{m}_{total} = 36.0$ and 35.6 g/s, where no counter-rotating waves were observed, the non-dimensional fill height was particularly high. Furthermore, based on the observations in Figures 8, 10 , 15 , and 18, it was suggested that the total mass flow rate and equivalence ratio have a more significant influence than the ignition method on the establishment of rotating detonation waves at the steady state.

Evaluation of detonation initiation success

To demonstrate the successful operation of the laser-ignited RDE, the detonation initiation success was evaluated based on the detonation propagation assessments at the steady state. Based on the two non-dimensional indicators discussed in the previous sections, detonation initiation success was evaluated as follows: Cases satisfying both criteria, i.e. $u/u_{CJ} > 0.6$ and $h/\lambda > 3$ for all measurements, were classified as "fully successful in establishing detonations." Cases satisfying only one of these criteria were classified as "partially successful in establishing detonations," while the remaining cases were classified as "failure to establish detonations."

As shown in Figure 19, although ignition success was achieved in all test cases, fully successful detonation establishment was achieved at $\dot{m}_{total} = 32.1$, 36.0, 45.0, and 45.0 g/s with corresponding equivalence ratios of $ER = 0.92$, 0.98, 0.85, and 1.32 in the LAI configuration. In the LSI configuration, fully successful detonation establishment was achieved at $\dot{m}_{total} = 35.6$ g/s with $ER = 0.97$. Therefore, successful operation of laser-ignited RDE was demonstrated for both LAI and LSI under the respective operating conditions described

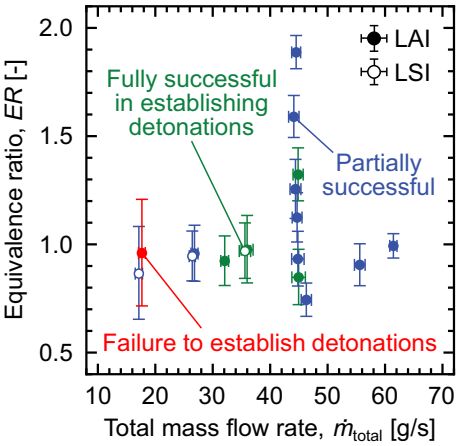


Figure 19. Detonation initiation success map. The green circles indicate cases satisfying both criteria of $u/u_{CJ} > 0.6$ and $h/\lambda > 3$, classified as "fully successful in establishing detonation." The blue circles indicate cases satisfying either criterion, classified as "partially successful in establishing detonation." The red circle indicates a case satisfying neither criterion, classified as "failure to establish detonation." The closed and open circles represent LAI and LSI cases, respectively.

above. Although further experiments under identical operating conditions are required, the present results suggest that the mass flow rate and equivalence ratio have a greater influence than the ignition method on the establishment of rotating detonation waves. Therefore, RDEs in the LSI configuration are expected to operate under similar conditions to those in the LAI configuration.

Simplified analysis of flame kernel development and ignition success

To explain why ignition success was achieved in all test cases, a simplified analysis of flame kernel development was conducted following previous studies (Endo et al. 2018; Eto et al. 2022). First, assuming that the unburned gas flow inside the annular channel had a uniform z-direction velocity component of $U_{\mathrm{fill}}\sin\theta_{\mathrm{fill}}$, as shown in Figure 17, the Reynolds number of the flow, Re, was calculated using the following equation:

$$Re = \frac{U_{\mathrm{fill}} \sin\theta_{\mathrm{fill}} D_{\mathrm{H}}}{\nu} \tag{22}$$

where D_{H} is the hydraulic diameter of the annular channel, defined as $D_{\mathrm{H}} = D_{\mathrm{out}} - D_{\mathrm{in}}$, and ν is the kinetic viscosity of the flow. Because the turbulent flowfield in an annular channel is difficult to describe analytically, the channel geometry was approximated as an equivalent circular pipe with the same hydraulic diameter. This approach is commonly used for estimating characteristic turbulent parameters, e.g. the turbulence intensity and integral length scale. All flow parameters related to the unburned gas in this section were calculated based on the mean compensated mass flow rate, temperature, and pressure during the 20 ms preceding ignition. The calculated Reynolds numbers ranged from $Re = 1.3 \times 10^5$ to 2.1×10^5, which exceeded the transition threshold of 5×10^3 (Green and Perry 2019), indicating that ignition occurred under turbulent flow conditions.

Next, the Fanning friction factor, F, was calculated using Prandtl's universal law of friction for smooth pipes (Schlichting and Gersten 2017). The Fanning friction factor relates the characteristic flow velocity to the wall shear stress and is used to estimate the wall friction velocity, which is required for evaluating the turbulence intensity. The Fanning friction factor was calculated from the Reynolds number obtained above using the following equation:

$$\frac{1}{\sqrt{4F}} = 2.0\log_{10}\left(Re\sqrt{4F}\right) - 0.8 \tag{23}$$

Note that the same equivalent circular pipe approximation described above was applied for the estimation of the friction factor. Then, the friction velocity, u_τ, was calculated from the Fanning friction factor as a characteristic velocity scale for estimating the turbulence intensity (Schlichting and Gersten 2017):

$$u_\tau = \sqrt{\frac{\tau}{\rho_\mathrm{u}}} \tag{24}$$

$$\tau = \tfrac{1}{2} F \rho_\mathrm{u} (U_\mathrm{fill} \sin\theta_\mathrm{fill})^2 \tag{25}$$

where, τ is the wall shear stress and ρ_u is the density of the unburned gas flow. The calculated friction velocity ranged from $u_\tau = 9.4$ to 15.4 m/s, which is consistent with the order of magnitude reported by Tobias et al. (2020). Finally, the turbulent integral length scale, l_E, was calculated using the empirical equation proposed by Adbel-Gayed and Bradley (1980):

$$l_\mathrm{E} = 0.08 D_\mathrm{H} \tag{26}$$

The friction velocity and integral length scale were then normalized using the laminar burning velocity, S_L, and laminar flame thickness, δ_F, respectively, which were calculated using Cantera (Goodwin et al. 2023) under the pre-ignition flow conditions. For simplicity, it was assumed that the injected propellants were sufficiently mixed before reaching the ignition point.

Finally, the turbulent first Damköhler number, Da_I, was calculated:

$$Da_\mathrm{I} = \frac{t_\mathrm{t}}{t_\mathrm{ch}} = \frac{l_\mathrm{E}/u_\tau}{\delta_\mathrm{F}/S_\mathrm{L}} \tag{27}$$

The Damköhler number is defined as the ratio of characteristic timescales between turbulence and chemical reaction, $t_\mathrm{t}/t_\mathrm{ch}$, and $Da_\mathrm{I} = 1$ indicates that the turbulence and chemical reaction have comparable contributions to flame development. However, $Da_\mathrm{I} = 1$ is not a universal criterion to account for the ignition success for the following reasons. First, the critical Damköhler number depends on the flowfield geometry, flow conditions, and ignition configuration, and critical values different from $Da_\mathrm{I} = 1$ have been reported (Biswas et al. 2016; Chi et al. 2022). In addition, flame kernel development in the present study was also considered to be influenced by other factors not explicitly included in the definition of the Damköhler number, e.g. local mixing effects, plasma size, electron temperature, and the surface area of the initial flame kernel. Nevertheless, the Damköhler number still provides useful insight into the relative timescales of turbulence and chemical

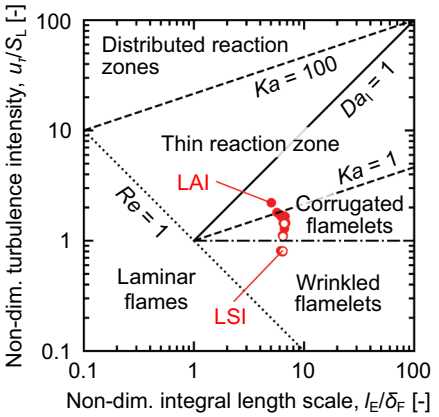


Figure 20. The regime diagram of the turbulent combustion. The red plots denote the tested 29 cases, where the closed and open circles represent LAI and LSI, respectively. The positively sloped solid line indicates $Da_I = 1$; regimes below this line, including the corrugated flamelets and wrinkled flamelets, correspond to $Da_I > 1$. The dashed lines indicate constant Karlovitz numbers and separate the distributed reaction zones, thin reaction zone, and corrugated flamelets. The negatively sloped dotted line indicates $Re = 1$, representing the boundary of the laminar flames. The horizontal dash-dotted line indicates $u_\tau/S_L = 1$, which separates the corrugated flamelets and wrinkled flamelets.

reactions, and $Da_I \approx 1$ can be regarded as an order-of-magnitude indicator for identifying conditions where the two characteristic timescales become comparable.

The non-dimensional friction velocity, u_τ/S_L, the non-dimensional turbulent integral length scale, l_E/δ_F, and the turbulent first Damköhler number, Da_I, for all test cases were plotted on the regime diagram of turbulent combustion proposed by Peters (1988), as shown in Figure 20. The turbulent first Damköhler number ranged from $Da_I = 2.3$ to 5.9, and most cases were located in the regime of corrugated flamelets, characterized by $Da_I > 1$ and $Ka < 1$. Note that Ka is the Karlovitz number, representing the ratio of the chemical reaction timescale to the smallest turbulent timescale associated with flame stretching. In the regime of corrugated flamelets, the flame surface is wrinkled, while the influence of turbulence on the inner flame structure is negligible. In other words, the present results suggest that the turbulence intensity did not significantly hinder the growth of the initial flame kernels, allowing them to develop into self-sustained combustion waves and resulting in ignition success.

Conclusions

In the present study, the feasibility of laser ignition as a potential ignition method for rotating detonation engines was demonstrated using laser ablation ignition and laser-induced spark ignition configurations. A total of 29 test cases were conducted using gaseous hydrogen and oxygen under total mass flow rates of $\dot{m}_{total} = 17.1 - 61.5$ g/s and equivalence ratios of $ER = 0.74 - 1.89$, corresponding to oxidizer-to-fuel ratios of $ROF = 4.2 - 10.7$, leading to the following findings:

- First, ignition success was achieved in all test cases. In the burst-mode tests, ignition was successfully achieved following the first pulse. Despite the observed laser ablation mark, the test campaign was completed without significant structural degradation of the ignition system or combustion chamber. These results demonstrated the robustness of the laser ignition system for repeated operation.
- Second, high-speed camera images were used to investigate flame kernel development and combustion wave propagation. Although laser ablation ignition and laser-induced spark ignition produced different initial flame kernel morphologies, the flowfields became comparable after approximately 100 μs, indicating that the influence of the ignition method was limited to the initial stage of flame development.
- Third, the detonation propagation at the steady state was assessed using the non-dimensional propagation velocity of the rotating chemiluminescence pattern, u/u_{CJ}. The non-dimensional velocity was generally independent on the ignition method, indicating that the detonation propagation at the steady state was governed primarily by the operating conditions rather than the ignition configuration. In the laser ablation configuration, the highest non-dimensional velocity was obtained at $\dot{m}_{total} = 36.0$ g/s, after which it decreased with increasing total mass flow rate and equivalence ratio.
- Fourth, the detonation propagation at the steady state was assessed based on the non-dimensional maximum fill height of the unburned gas, h/λ. At $\dot{m}_{total} = 36.0$ g/s, the non-dimensional fill height fell within the empirical operational range of rotating detonation engines, $h/\lambda = 12 \pm 5$, and approached the empirical threshold for high-probability detonation sustainment, $h/\lambda = 3$, as the total mass flow rate deviated from $\dot{m}_{total} = 36.0$ g/s. At $\dot{m}_{total} = 44.8$ g/s, the non-dimensional fill height remained close to the empirical threshold near the stoichiometric condition and became smaller as the equivalence ratio deviated from stoichiometry.
- Fifth, and most importantly, detonation initiation success was evaluated based on the aforementioned non-dimensional indicators. Using $u/u_{CJ} > 0.6$ and $h/\lambda > 3$ as the criteria for fully successful detonation initiation, laser ablation ignition satisfied these criteria at $\dot{m}_{total} = 32.1$, 36.0, 45.0, and 45.0 g/s, corresponding to equivalence ratios of $ER = 0.92$, 0.98, 0.85, and 1.32, respectively. Laser-induced spark ignition satisfied the same criteria at $\dot{m}_{total} = 35.6$ g/s with $ER = 0.97$. Therefore, successful operation of the laser-ignited rotating detonation engine was demonstrated for both laser ablation ignition and laser-induced spark ignition under the respective operating conditions described above.
- Finally, the relative influence of turbulence and chemical reactions on flame kernel development in the pre-ignition flow was analyzed to explain the observed ignition success. Ignition was achieved under turbulent flow conditions, with turbulent first Damköhler numbers ranging from $Da_I = 2.3$ to 5.9, suggesting that the turbulence intensity was insufficient to significantly disrupt the flame kernel development. It should be noted, however, that the analysis was simplified by neglecting the mixing of the injected propellants, and therefore should be regarded as a first-order interpretation of the ignition success mechanism.

Although the applicability of these conclusions may be limited to the tested device, this study demonstrates the feasibility of laser ignition as an alternative method for starting rotating detonation engines. Therefore, further investigations are needed for the practical

application of laser-ignited rotating detonation engines, including clarification of the detailed mechanism of the initial process following laser irradiation, optimization of the optical pathways for quicker detonation establishment with higher reliability, and comparisons with the conventional ignition methods.

Nomenclature

A [m^2]	Total injection area
a [m/s]	Sound speed of the burned gas
C_d [–]	Discharge coefficient
CCW	Rotation in counterclockwise direction
CJ	Chapman-Jouguet state
CW	Rotation in clockwise direction
c_p [J/kg K]	Isobaric specific heat
D [m]	Diameter of the annular channel
D_H [m]	Hydraulic diameter of the annular channel
D_{in} [m]	Inner diameter of the annular channel
D_{mean} [m]	Mean diameter of the annular channel
D_{out} [m]	Outer diameter of the annular channel
Da [–]	Turbulent first Damköhler number
d [m]	Focused beam diameter
d_0 [m]	Beam waist diameter
d_{in} [m]	Input laser beam diameter
E_{in} [J]	Laser pulse energy
ER [–]	Equivalence ratio
F [–]	Fanning friction factor
FWHM	Full width at half maximum
f [Hz]	Frequency
f_{axial} [Hz]	Axial resonant frequency
f_{azm} [Hz]	Azimuthal resonant frequency
f_{peak} [Hz]	Peak frequency in the pressure and light intensity spectrograms
f_{rad} [Hz]	Radial resonant frequency
h [m]	Maximum fill height of the unburned gas
Ka [–]	Karlovitz number
L [m]	Combustion chamber length
LAI	Laser ablation ignition
LSI	Laser-induced spark ignition
l [m]	Axial distance from the laser beam waist
l_E [m]	Turbulent integral length scale
l_F [m]	Focal length of the focusing lens
l_R [m]	Rayleigh length
M^2 [–]	Beam quality factor
$\dot{m}$ [kg/s]	Mass flow rate measured by the mass flowmeter
$\dot{m}_{fill}$ [kg/s]	Mass flow rate of the unburned gas filled into the combustion chamber
$\dot{m}_{fu}$ [kg/s]	Measured mass flow rate of the fuel

$\dot{m}_{ox}$ [kg/s]	Measured mass flow rate of the oxidizer
$\dot{m}_c$ [kg/s]	Compensated mass flow rate
$\dot{m}_{c,fu}$ [kg/s]	Compensated mass flow rate of the fuel
$\dot{m}_{c,ox}$ [kg/s]	Compensated mass flow rate of the oxidizer
$\dot{m}_{total}$ [kg/s]	Total mass flow rate
N [–]	Number of the rotating chemiluminescence pattern
N_{CW} [–]	Number of the chemiluminescence pattern rotating in clockwise direction
N_{CCW} [–]	Number of the chemiluminescence pattern rotating in counter-clockwise direction
n [–]	Acoustic mode number
OP	Optical probe
PE	Piezo-electric pressure sensor
PR	Piezo-resistive pressure sensor
p_0 [Pa]	Plenum pressure
p_{cc} [Pa]	Combustion chamber pressure
q_m [J/kg]	Latent heat of fusion
R [J/kg K]	Gas constant of the propellant
RDE	Rotating detonation engine
Re [–]	Reynolds number of the unburned gas flow
ROF [–]	Mass-based oxidizer-to-fuel ratio
r [m]	Radial axis of the combustion chamber
S_L [m/s]	Laminar burning velocity
T [K]	Temperature
T_0 [K]	Plenum temperature
T_{bg} [K]	Background temperature
TC	Thermocouple
T_m [K]	Melting point of the inner body material
t [s]	Elapsed time after ignition
t_{ch} [s]	Characteristic timescale of chemical reaction
t_t [s]	Characteristic timescale of turbulence
Δt_{fill} [s]	Unburned gas fill time
Δt_{FWHM} [s]	Laser pulse width (FWHM of laser pulse peak power)
Δt_{trg} [s]	Period of time from the run-valve opening to the laser triggering
U [m/s]	Velocity of the propellant jet
U_{fill} [m/s]	Velocity of the unburned gas filled into the combustion chamber
U_{fu} [m/s]	Velocity of the fuel jet
U_{ox} [m/s]	Velocity of the oxidizer jet
u [m/s]	Velocity of the rotating chemiluminescence pattern
u_{CJ} [m/s]	Chapman-Jouguet detonation speed
u_{CW} [m/s]	Velocity of the chemiluminescence pattern rotating in clockwise direction
u_{CCW} [m/s]	Velocity of the chemiluminescence pattern rotating in counterclockwise direction
u_τ [m/s]	Friction velocity of the unburned gas flow
z [m]	Longitudinal axis of the combustion chamber

α [m^2/s]	Thermal diffusivity of the inner body material
γ [–]	Specific heat ratio
δ_F [m]	Laminar flame thickness
δ_{opt} [m]	Optical skin depth
δ_{melt} [m]	Theoretical melt depth
δ_{th} [m]	Thermal diffusion length
δ [-]	Laser absorption coefficient
θ [rad]	Angle of the propellant jet
θ_{fill} [rad]	Angle of the unburned gas filled into the combustion chamber
θ_{fu} [rad]	Angle of the fuel jet
θ_{ox} [rad]	Angle of the oxidizer jet
Λ [m]	Wavelength of the laser beam
λ [m]	Detonation cell width
ν [m^2/s]	Kinetic viscosity of the unburned gas flow
Π [-]	Critical pressure ratio between the chamber and plenum
ρ_{IB} [kg/m^3]	Density of the inner body material
ρ_u [kg/m^3]	Density of the unburned gas flow
σ [–]	Stability of the rotating chemiluminescence pattern
σ_{CW} [–]	Stability of the chemiluminescence pattern rotating in clockwise direction
σ_{CCW} [–]	Stability of the chemiluminescence pattern rotating in counterclockwise direction
τ [N/m^2]	Shear stress on the channel wall

Acknowledgements

The authors also gratefully thank Kilian Rheindorf for the image analysis, Markus Dengler for the technical support at the test facility, and Stephan General, Bernhard Knapp, and Leon Lober for the support in the high-speed camera recording.

Author contributions

CRediT: **Tomoyuki Sato:** Conceptualization, Formal analysis, Funding acquisition, Investigation, Methodology, Software, Validation, Visualization, Writing – original draft; **Michael Börner:** Conceptualization, Data curation, Funding acquisition, Investigation, Methodology, Resources, Supervision, Writing – review & editing; **Wolfgang Armbruster:** Investigation, Methodology, Resources, Writing – review & editing; **Alexander Bee:** Data curation, Methodology, Resources; **Maria Giulia Monti:** Methodology, Resources; **Justin Hardi:** Funding acquisition, Project administration, Writing – review & editing.

Disclosure statement

No potential conflict of interest was reported by the author(s).

Funding

This study was supported by JSPS Overseas Research Fellowships.

ORCID

Tomoyuki Sato http://orcid.org/0009-0002-0698-6117
Michael Börner http://orcid.org/0000-0002-3441-2869
Wolfgang Armbruster http://orcid.org/0000-0002-4859-4173
Alexander Bee http://orcid.org/0000-0002-4456-8082
Maria Giulia Monti http://orcid.org/0009-0000-0525-8420
Justin Hardi http://orcid.org/0000-0003-3258-5261

References

Adbel-Gayed RG, Bradley D. 1980. Turbulent length scales and the turbulent transport number for isotropic turbulence. J Fluids Eng. 102(3):389. https://doi.org/10.1115/1.3240708

Anand V, George AS, Driscoll R, Gutmark E. 2016. Investigation of rotating detonation combustor operation with H_2-air mixtures. Int J Hydrogen Energy. 41(2):1281–1292. https://doi.org/10.1016/j.ijhydene.2015.11.041

Anderson WS, Heister SD, Kan B, Hartsfield C. 2020. Experimental study of a hypergolically ignited liquid bipropellant rotating detonation rocket engine. J Propuls Power. 36:851–861. https://doi.org/10.2514/1.B37666

Armbruster W et al. 2025. Design and testing of a hydrogen–oxygen pre-detonator for rotating detonation engines. CEAS Space J. 17(6):969–979. https://doi.org/10.1007/s12567-025-00605-y

Armbruster W et al. 2026. Visualization of the detonation wave structure in a small-scale hydrogen–oxygen rotating detonation combustor. Aerospace. 13(2):158. https://doi.org/10.3390/aerospace13020158

Bai Q, Han J, Zhang S, Weng C. 2023. Experimental study on the auto-initiation of rotating detonation with high-temperature hydrogen-rich gas. Phys Fluids. 35:045121. https://doi.org/10.1063/5.0144322

Baumann R, Hipp D, Lasagni AF, Mahrle A. 2021. Tailored absorptivity: increasing the laser weldability of copper through surface structuring. Mater Lett. 283:128700. https://doi.org/10.1016/j.matlet.2020.128700

Bennewitz JW, Bigler BR, Schumaker SA, Hargus WA. 2019. Automated image processing method to quantify rotating detonation wave behavior. Rev Sci Instrum. 90(6):065106. https://doi.org/10.1063/1.5067256

Biswas S, Tanvir S, Wang H, Qiao L. 2016. On ignition mechanisms of premixed CH_4/air and H_2/air using a hot turbulent jet generated by pre-chamber combustion. Appl Therm Eng. 106:925–937. https://doi.org/10.1016/j.applthermaleng.2016.06.070

Börner M. 2022. Experimentelle Untersuchung der laserinduzierten Zündung von kryogenen Flüssigkeitsraketenbrennkammern [dissertation]. RWTH Aachen University. https://doi.org/10.57676/p7c7-dn53

Börner M, Manfletti C, Kroupa G, Oschwald M. 2017. Repetitive laser ignition by optical breakdown of a LOX/H_2 rocket combustion chamber with multi-injector head configuration. CEAS Space J. 9(3):289–297. https://doi.org/10.1007/s12567-017-0163-7

Brieschenk S, O'byrne S, Kleine H. 2013. Laser-induced plasma ignition studies in a model scramjet engine. Combust Flame. 160(1):145–148. https://doi.org/10.1016/j.combustflame.2012.08.011

Burke MP, Chaos M, Ju Y, Dryer FL, Klippenstein SJ. 2011. Comprehensive H_2/O_2 kinetic model for high-pressure combustion. Int J Chem Kinet. 44(7):444–474. https://doi.org/10.1002/kin.20603

Bykovskii FA, Vasil'ev AA, Vedernikov EF, Mitrofanov VV. 1994. Explosive combustion of a gas mixture in radial annular chambers. Combust Explos Shock Waves. 30(4):510–516. https://doi.org/10.1007/BF00790158

Bykovskii FA, Zhdan SA, Vedernikov EF. 2006. Continuous spin detonations. J Propuls Power. 22(6):1204–1216. https://doi.org/10.2514/1.17656

Chi C, Abdelsamie A, Thévenin D. 2022. Transient ignition of premixed methane/air mixtures by a pre-chamber hot jet: a DNS study. Flow Turbul Combust. 108(3):775–795. https://doi.org/10.1007/s10494-021-00292-9

Connolly-Boutin S, Joseph V, Ng HD, Kiyanda CB. 2021. Small-size rotating detonation engine: scaling and minimum mass flow rate. Shock Waves. 31(7):665–674. https://doi.org/10.1007/s00193-021-00991-2

Denisov YN, Troshin YK. 1960. Structure of gaseous detonation in tubes. Sov Phys Tech Phys. 5 (4):419–431.

Desbordes D. 1990. Aspects stationnaires et transitoires de la detonation dans les gaz: relation avec la structure cellulaire du front [dissertation]. Universite de Poitiers.

Döring W. 1943. Über den Detonationsvorgang in Gasen [On the detonation process in a gas]. Ann Phys. 435(6–7):421–436. https://doi.org/10.1002/andp.19434350605

Endo T et al. 2018. Comparative study of laser ignition and spark-plug ignition in high-speed flows. Combust Flame. 191:408–416. https://doi.org/10.1016/j.combustflame.2018.01.029

Eto K, Kojima Y, Kim W, Johzaki T, Endo T. 2022 Jun 19–24. Comparison between laser ignition and spark-plug ignition of flowing propane-air mixtures. Paper presented at: 28th International colloquium on the dynamics of explosions and reactive systems. Naples, Italy.

Explosion Dynamics Laboratory. 2023. SDToolbox: numerical tools for shock and detonation wave modeling. Report No.: FM2018.001. California Institute of Technology.

Fickett W, Davis WC. 2000. Detonation: theory and experiment. Dover.

Goodwin DG, Moffat HK, Schoegl I, Speth RL, Weber BW. 2023. Cantera: an object-oriented software toolkit for chemical kinetics, thermodynamics, and transport processes. https://www.cantera.org Version 3.0.1.

Goto K et al. 2023. Space flight demonstration of rotating detonation engine using sounding rocket S-520-31. J Spacecr Rockets. 60:273–285. https://doi.org/10.2514/1.A35401

Green DW, Perry RH. 2019. Perry's chemical engineers' handbook. McGraw-Hill.

Guirao CM, Knystautas R, Lee JHS, Benedick W, Berman M. 1982. Hydrogen-air detonations. Symp (Int) Combust. 19(1):583–590. https://doi.org/10.1016/S0082-0784(82)80232-4

Hou Y, Sheng Z, Song Q, Ma JZ, Wang J. 2026. Flame acceleration and detonation re-initiation in non-premixed rotating detonation engines. AIAA J. 64(5):2620–2633. https://doi.org/10.2514/1.J066045

Jo S et al. 2026. Effects of chamber length on the structure of detonation waves in a non-premixed ethylene-oxygen rotating detonation engine. Phys Fluids. 38(3):036112. https://doi.org/10.1063/5.0308631

Kailasanath K. 2000. Review of propulsion applications of detonation waves. AIAA J. 38 (9):1698–1708. https://doi.org/10.2514/2.1156

Kaneshige MJ. 1999. Gaseous detonation initiation and stabilization by hypervelocity projectiles [dissertation]. California Institute of Technology.

Kaneshige MJ, Shepherd JE. 1997. Detonation database. California Institute of Technology. Report No.: FM97-8.

Kindracki J, Wolanski P, Gut Z. 2011. Experimental research on the rotating detonation in gaseous fuels–oxygen mixtures. Shock Waves. 21(2):75–84. https://doi.org/10.1007/s00193-011-0298-y

Knystautas R, Lee JHS, Guirao CM. 1982. The critical tube diameter for detonation failure in hydrocarbon-air mixtures. Combust Flame. 48:63–83. https://doi.org/10.1016/0010-2180(82)90116-X

Koch J, Kurosaka M, Knowlen C, Kutz JN. 2021. Multiscale physics of rotating detonation waves: autosolitons and modulational instabilities. Phys Rev E. 104(2):024210. https://doi.org/10.1103/PhysRevE.104.024210

Kroupa G, Börner M. 2019. A miniaturized high energy laser for ignition of rocket engines. In: Sodnik Z, Karafolas N, Cugny B editors. International Conference on Space Optics; 2018 Oct 9–12; Chania, Greece. SPIE. p 111805I.

Kroupa G, Tabakaev D, Börner M, Rackemann N, Soller S. 2024. Overview and recent applications of the miniaturized HiPoLas ignition system. Opt Express. 32(24):42289–42300. https://doi.org/10.1364/OE.539141

Kudo Y, Nagura Y, Kasahara J, Sasamoto Y, Matsuo A. 2011. Oblique detonation waves stabilized in rectangular-cross-section bent tubes. Proc Combust Inst. 33(2):2319–2326. https://doi.org/10.1016/j.proci.2010.08.008

Lee JHS, Matsui H. 1977. A comparison of the critical energies for direct initiation of spherical detonation in acetylene-oxygen mixtures. Combust Flame. 28:61–66. https://doi.org/10.1016/0010-2180(77)90008-6

Li X, Liu W, Pan Y, Yang L, An B. 2017. Experimental investigation on laser-induced plasma ignition of hydrocarbon fuel in scramjet engine at takeover flight conditions. Acta Astronaut. 138:79–84. https://doi.org/10.1016/j.actaastro.2017.05.036

Lin W, Zhou J, Liu S, Lin Z. 2015. An experimental study on CH_4/O_2 continuously rotating detonation wave in a hollow combustion chamber. Exp Therm Fluid Sci. 62:122–130. https://doi.org/10.1016/j.expthermflusci.2014.11.017

Liou LC. 1984 Jun 27–29. Laser ignition in liquid rocket engines. Paper presented at: 30th AIAA/SAE/ASME/ASEE Joint Propulsion Conference; Indianapolis, IN, United States.

Liu Y-F, Shen H, Zhang D-L, Jiang Z-L. 2018. Theoretical analysis on deflagration-to-detonation transition. Chi Phys B. 27(8):084703. https://doi.org/10.1088/1674-1056/27/8/084703

Manzhalei VI, Mitrofanov VV, Subbotin VA. 1974. Measurement of inhomogeneities of a detonation front in gas mixtures at elevated pressures. Combust Explos Shock Waves. 10:89–95. https://doi.org/10.1007/BF01463793

Michalski Q et al. 2024. Structure of rotating detonation in mixtures of natural gas and oxygen. Combust Flame. 260:113253. https://doi.org/10.1016/j.combustflame.2023.113253

Morgan CG. 1975. Laser-induced breakdown of gases. Rep Prog Phys. 38(5):621. https://doi.org/10.1088/0034-4885/38/5/002

Mori K et al. 2003. Ignition characteristics of GH_2/GO_x mixture using laser ablation ignition. Trans Jpn Soc Mech Eng. 46(152):121–126. https://doi.org/10.2322/tjsass.46.121

Morishita N et al. 2022. Development of a laser ignition system for a solid rocket motor on the OMOTENASHI spacecraft. Sci Technol Energ Mater. 83(2):59–64. https://doi.org/10.34571/stem.83.2_59

Nicholls JA, Cullen RE, Ragland KW. 1966. Feasibility studies of a rotating detonation wave rocket motor. J Spacecr Rockets. 3(6):893–898. https://doi.org/10.2514/3.28557

Peters N. 1988. Laminar flamelet concepts in turbulent combustion. Symp (Int) Combust. 21(1):1231–1250. https://doi.org/10.1016/S0082-0784(88)80355-2

Phuoc TX, White CM. 2000. Experimental studies of the absorption and emissions from laser-induced spark in combustible gases. Opt Commun. 181(4–6):353–359. https://doi.org/10.1016/S0030-4018(00)00770-7

Pretto M, Betta ED, Giannattasio P. 2024. Estimating the minimum ignition energy of spark-ignited fuel/air mixtures: preliminary steps towards a novel modelling approach. J Phys Conf Ser. 2893:012093. https://doi.org/10.1088/1742-6596/2893/1/012093

Rankin BA et al. 2016. Evaluation of mixing processes in a non-premixed rotating detonation engine using acetone PLIF. Paper presented at: 54th AIAA Aerospace Sciences Meeting; San Diego, CA, United States.

Ronney PD. 1994. Laser versus conventional ignition of flames. Opt Eng. 33(2):510–521. https://doi.org/10.1117/12.152237

Saleh BEA, Teich MC. 2019. Fundamentals of photonics. 3rd ed. Wiley.

Schlichting H, Gersten K. 2017. Boundary-layer theory. Springer.

Stevens CA, Fotia M, Hoke J, Schumaker SA. 2021. January 11–15 and 19–21. The effect of ignition pressure pulse on light-off in an RDE. Paper presented at: AIAA Science and Technology Forum; Virtual event.

Strehlow RA. 1969. Transverse waves in detonations: ii. structure and spacing in H_2–O_2, C_2H_2–O_2, C_2H_4–O_2 and CH_4–O_2 systems. AIAA J. 7(3):492–496. https://doi.org/10.2514/3.5134

Takahashi E, Kato S. 2021. Laser ablation ignition of flammable gas. Jpn J Appl Phys. 60(4):047001. https://doi.org/10.35848/1347-4065/abed20

Tobias JR, Miller RS, Agrawal AK. 2020 Aug 24–28. Flow measurements inside a rotating detonation chamber. Paper presented at. AIAA Propulsion and Energy Forum; Virtual event.

Voitsekhovskii BV. 1960. Stationary spin detonation. Sov J Appl Mech Technol Phys. 3:157–164.
Voitsekhovskii BV, Mitrofanov VV, Topchian ME. 1966. The structure of a detonation front in gases. Wright-Patterson Air Force Base. Report No.: FTD-MT-64-527.
Wang Y, Wang J. 2015. Effect of equivalence ratio on the velocity of rotating detonation. Int J Hydrogen Energy. 40(25):7949–7955. https://doi.org/10.1016/j.ijhydene.2015.04.072
Weber KD, Fievisohn RT, Blunck DL. 2025. Evaluating the effects of fill height in a narrow detonation channel. J Propuls Power. 41(5):578–588. https://doi.org/10.2514/1.B39777
Wolański P. 2013. Detonative propulsion. Proc Combust Inst. 34(1):125–158. https://doi.org/10.1016/j.proci.2012.10.005
Yang C, Wu X, Ma H, Peng L, Gao J. 2016. Experimental research on initiation characteristics of a rotating detonation engine. Exp Therm Fluid Sci. 71:154–163. https://doi.org/10.1016/j.expthermflusci.2015.10.019
Zitoun R, Desbordes D, Guerraud C, Deshaies B. 1995. Direct initiation of detonation in cryogenic gaseous H_2–O_2 mixtures. Shock Waves. 4(6):331–337. https://doi.org/10.1007/BF01413875